UNIVERSITY OF CALIFORNIA
RIVERSIDE

Computational Study of Large-Scale Graphdiyne Nanotubes and Quantum Mechanical Methods in Sulfate Radical Oxidation

A Thesis submitted in partial satisfaction
of the requirements for the degree of

Master of Science

in

Chemical and Environmental Engineering

by

Sangavi Pari

June 2017

Thesis Committee:
Dr. Bryan M. Wong, Chairperson
Dr. Haizhou Liu
Dr. Jianzhong Wu

The Thesis of Sangavi Pari is approved:

Committee Chairperson

University of California, Riverside

ACKNOWLEDGEMENTS OF THE THESIS

I acknowledge all previously published material, co-authors of my thesis material, and financial support received for my thesis. My thesis comprises of two projects that have distinct publications, collaborations, and funding.

My first project, titled "Structural and Electronic Properties of Graphdiyne Carbon Nanotubes from Large-Scale DFT Calculations", was previously published in the *Journal of Physical C* in August 2016. The entire article, without being rewritten, is represented as Chapter 1 in my thesis. The supplemental figures accompanied in the publication are also included, without revision, in the appendix section. I thank my co-authors Abigail Cuéllar and Bryan M. Wong for their collaboration. I also want to acknowledge the National Science Foundation for funding our use of supercomputing resources under the Extreme Science and Engineering Discovery Environment (XSEDE), Project No. TG-CHE150040.

My second project, titled "Sulfate radical oxidation of aromatic contaminants: a detailed assessment of density functional theory and high-level quantum chemical methods", was previously published in *Environmental Science: Processes & Impacts* in February 2017. The entire article, without being rewritten, is represented as Chapter 2 in my thesis. I again would like to thank my co-workers Inger A. Wang, Haizhou Liu, and Bryan M. Wong for their collaboration. Finally I would like to thank the National Science Foundation again, for funding our use of supercomputing resources under the Extreme Science and Engineering Discovery Environment (XSEDE), Project No. TG-CHE150040. Collaborator Wong and I were additionally supported by the U.S.

Department of Energy, Office of Science, Early Career Research Program under Award No. DE-SC0016269. Collaborators Wang and Liu were supported under the National Science Foundation through the Research Experiences for Undergraduates (REU) program (ACI-1452367) and National Science Foundation (CHE-1611306), respectively. I would also like to thank the Royal Society of Chemistry for featuring our article as a cover issue in *Environmental Science: Processes & Impacts*.

Table of Contents

Introduction……1

Chapter 1: Structural and Electronic Properties of Graphdiyne Carbon Nanotubes from Large-Scale DFT Calculations

Title……3
Abstract……3
Introduction……4
Structural Properties of Graphdiyne Nanotubes……7
Theory and Methodology……8
Results and Discussion……10
Conclusion……22
References……24

Chapter 2: Sulfate Radical Oxidation of Aromatic Contaminants: A Detailed Assessment of Density Functional Theory and High-Level Quantum Chemical Methods

Title……28
Abstract……28
Introduction……29
Computational Methods……33
Results and Discussion……35
Conclusions……45
References……47

Conclusion……55

Appendix……57

List of Figures

Figure 1.1……...……..6
Chemical structures and unit cells for graphene, α-graphyne, and graphdiyne. All structures and unit cells are drawn to scale, with each unit cell containing 2, 8, and 18 carbon atoms for graphene, α-graphyne, and graphdiyne, respectively.

Figure 1.2……..……7
Optimized structures of the (3,3) zigzag and (5,0) armchair graphdiyne nanotubes.

Figure 1.3……..……8
Lattice vectors $\vec{a}_1$ and $\vec{a}_2$, chiral angle θ, and selected chiral vectors (3,0) and (2,2) for a graphydiyne sheet.

Figure 1.4……..……..11
Electronic band structure for planar graphdiyne obtained at the HSE06/TZVP level of theory. The dashed horizontal line indicates the position of the Fermi energy, and a direct bandgap of 1.26 eV occurs at the Γ point within the irreducible Brillouin zone.

Figure 1.5……..……14
Relaxation energy, ΔE, as a function of diameter for both armchair and zigzag GDNTs obtained at the HSE06/TZVP level of theory.

Figure 1.6……..……15
Electronic band structures (relative to vacuum at 0 eV) of various (n,0) armchair GDNTs for n = 2, 13, 24, and 36. Note the narrow (and nearly dispersionless) bands for the (2,0) GDNT.

Figure 1.7……..……..15
Electronic band structures (relative to vacuum at 0 eV) of various (n,n) zigzag GDNTs for n = 2, 8, 14, and 21. Note that the zigzag GDNTs have wider valence and conduction bands compared to their armchair GDNT counterparts.

Figure 1.8……..……19
Electronic bandgap as a function of diameter for both armchair and zigzag GDNTs obtained at the HSE06/TZVP level of theory.

Figure 1.9……..……21
Highest occupied and lowest unoccupied crystal orbitals (HOCO and LUCO) for the (5,0) armchair and (3,3) zigzag GDNTs (only crystal orbitals within one unit cell are shown for clarity). Both the HOCO and LUCO are localized along acetylenic linkages along the circumference of the (5,0) GDNT, whereas the HOCO and LUCO are localized along acetylenic linkages along the axis of the (3,3) GDNT.

Figure 1.10……22
Projected density of states for the (3,3) zigzag and (5,0) armchair GDNT. For both the (3,3) and (5,0) GDNT, the carbon p orbitals contribute a significant fraction of the total density of states.

Figure 2.1……..32
Chemical structures of benzene-derived organic contaminants investigated in this work.

Figure 2.2……..33
Reaction steps investigated in this work: Step 1 involves the addition of $SO_4^{\bullet-}$ to form a benzene-derivative cation and the SO_4^{2-} anion. The *R* group represents the different functional groups depicted previously in Figure 2.1. Step 2 involves the addition of OH^- to the benzene-derivative cation that gives the final hydroxylated product.

Figure 2.3……..37
Comparison of (a) CCSD single-point energies on top of CCSD and M06-2X optimized geometries and (b) CCSD(T)/aug-cc-pvtz and CCSD(T)/6-311+G(d,p) single-point energies on top of M06-2X optimized geometries for 1-aminophenol. The insets in each of the figures show a magnified portion of the potential energy surface near the transition state, indicating a small energy difference among the various computational methods used in each of the figures.

Figure 2.4……..39
Reactants, transition states, and products for the first reaction step involving addition of $SO_4^{\bullet-}$ to toluene.

Figure 2.5……..40
Predicted activation energies of the (a) forward and (b) reverse reactions of various benzene derivatives reacting with $SO_4^{\bullet-}$. The diagonal line in each figure represents a perfect match to the benchmark CCSD(T) activation energies.

Figure 2.6……..42
Reactants and products for the second reaction step involving addition of OH^- to toluene.

Figure 2.7……43
All possible products resulting from the reaction of various hydroxylated oxidation products from oxidation of benzene derivatives by sulfate radical and subsequent OH^- addition. The energies of the various products were computed using both DFT and high-level wavefunction based methods to assess the accuracy of all the computational methods used in the main text.

Figure 2.8……..……44
Predicted activation energies of the (a) forward and (b) reverse reactions of benzene-derived cation radical reacting with OH^-. The diagonal line in each figure represents a perfect match to the benchmark CCSD(T) activation energies.

Figure 1.11……..……60
Electronic band structures (relative to vacuum at 0 eV) of various (*n*,0) armchair GDNTs for $n = 2 – 21$

Figure 1.12……61
Electronic band structures (relative to vacuum at 0 eV) of various (*n*,0) armchair GDNTs for $n = 22 – 36$

Figure 1.13……62
Electronic band structures (relative to vacuum at 0 eV) of various (*n*,*n*) zigzag GDNTs for $n = 2 – 21$

List of Tables

Table 1.1……...……16
Radii, Relaxation Energies, Binding Energies per Atom, Effective Electron Mass, Effective Hole Mass, and Bandgaps of Armchair Graphdiyne Nanotubes

Table 1.2……...……17
Radii, Relaxation Energies, Binding Energies Per Atom, Effective Electron Mass, Effective Hole Mass, and Bandgaps of Zigzag Graphdiyne Nanotubes

Table 2.1……40
Mean absolute error (MAE) with respect to CCSD(T) benchmarks and R^2 fit values for various activation energies (E_a) computed with the M06-2X, MP2, MP4(SDQ), and CCSD methods

Table 1.3……57
Vibrational frequencies, symmetries, and infrared/Raman analysis for the (2,2) GDNT. IRREP labels refer to the symmetry representation; A and I indicate whether the mode is active or inactive, respectively, for IR and Raman.

Introduction

Predictive simulations are used in a variety of disciplines to provide intuition in various engineering and scientific phenomena. Its versatility results from leveraging the speed and accuracy of computers to perform predictive calculations that can guide experimental efforts. My thesis involves two separate and distinct projects that highlight the use of computational chemistry for understanding the electronic properties of chemical and material systems. My first project involved using quantum calculations to investigate the electronic properties of graphdiyne nanotubes and my second project involved analyzing the accuracy and rigor of various quantum mechanical methods in predicting sulfate oxidation for water purification purposes.

My first project involved studying armchair and zigzag graphdiyne nanotubes. Specifically, we used the CRYSTAL14 software package to describe the one-dimensional structure of these graphdiyne nanotubes with large sizes (up to 1,296 atoms) and various diameters. These results were subsequently analyzed to predict various electronic properties (band gap, effective electron/hole mass) of the multiple graphdiyne nanotubes. The main purpose of this project was to provide computational predictions of these extremely large systems to study the electronic properties as a function of graphdiyne diameter.

My second project, which was featured as the cover issue of *Environmental Science: Processes & Impacts*, involved studying the accuracy of various DFT and high-level wavefunction-based methods in calculating activation energies for various benzene derived contaminants with sulfate ion and hydroxide. The computational methods used in

this project included the M06-2X, MP2, MP4(SDQ), CCSD, and CCSD(T) methods. The higher-level CCSD and CCSD(T) theoretically obtain more accurate energy values with a concurrent higher monetary cost. The CCSD(T) method was used as a benchmark to compare the accuracy of the other methods. The primary goal was to assess the accuracy of the computationally efficient M06-2X density function approach for various reactions involving sulfate oxidation.

Both of my projects involve predictive computational approaches for very different purposes. The scope of my first project was to determine how electronic properties varied as a function of diameter in armchair and zigzag graphdiyne nanotubes. My second project involved investigating the feasibility of multiple computational methods in accurately calculating reaction energy values, benchmarked by the highly accurate CCSD(T) method. Both of these projects highlight the importance of predictive quantum mechanical methods for both chemical and materials science applications.

Structural and Electronic Properties of Graphdiyne Carbon Nanotubes from Large-Scale DFT Calculations

Abstract. Using large-scale DFT calculations, we investigate the structural and electronic properties of both armchair and zigzag graphdiyne nanotubes as a function of size. To provide insight into these properties, we present new detailed calculations of the structural relaxation energy, effective electron/hole mass, and size-scaling of the bandgap as a function of size and chirality using accurate screened-exchange DFT calculations. These calculations provide a systematic evaluation of the structural and electronic properties of the largest graphdiyne nanotubes to date, up to 1,296 atoms and 23,328 basis functions. Our calculations show that zigzag graphdiyne nanotubes (GDNTs) are structurally more stable compared to armchair GDNTs of the same size. Furthermore, these large-scale calculations allow us to present simple analytical formulas to guide future experimental efforts for estimating the fundamental bandgaps of these unique nanotubes as a function of chirality and diameter. While the bandgaps for both the armchair and zigzag GDNTs can be tuned as a function of size, the conductivity in each of these two different chiralities is markedly different. Zigzag GDNTs have wider

valence and conduction bands and are expected to have a higher electron- and hole-mobility than their armchair counterparts.

I. Introduction

Carbon nanotubes and related allotropes continue to garner immense interest due to the unique electronic properties that naturally arise from their intrinsic one-dimensional nature.[1] Specifically, one-dimensional nanosystems (such as nanowires and nanotubes) are the smallest dimensions that can be used for efficient transport of electrons and are, therefore, critical to the functionality of nanoscale devices.[2] Within the carbon nanotube family, these devices have included field effect transistors,[3-8] actuators,[9, 10] nanotube films for flexible displays,[11] and nanotube hybrid solar panels.[12] In many of these devices, carbon nanotubes of a specific chirality (or a narrow range of chiralities possessing similar electronic properties) are often required. Within a normal distribution of carbon nanotube chiralities, roughly one-third of nanotubes are metallic, while the other two-thirds exhibit semiconducting behavior.[13] Because of this wide variation in carbon nanotube chiralities, recent efforts have focused on other allotropes of carbon to achieve a detailed control over their electronic properties and device functionality.

In recent years, much effort has focused on graphdiyne (cf. Figure 1.1), which is a new allotrope of carbon composed of two acetylenic linkages (with sp-hybridized carbon atoms) between nearest-neighbor hexagonal rings (composed of sp2-hybridized carbons). Planar graphdiyne exhibits a high-temperature stability and semiconducting properties comparable to silicon[14] and has been proposed for gas separation applications,[15]

nanoscale devices,[16] photocatalysts for hydrogen production,[17] and hydrogen purification in syngas production.[18] In a relatively recent report,[19] the experimental synthesis and construction of graphdiyne nanotubes (GDNTs, see Figure 1.2) were carried out for the very first time, and subsequent papers on other graphdiyne-based nanostructures have reported unique electronic properties, including charge mobilities as high as 2×10^5 cm^2 V^{-1} s^{-1} at room temperature.[20] However, to the best of our knowledge, a systematic study on the structural and electronic properties of GDNTs as a function of size and chirality has not been previously reported. To provide insight into these properties, we present a new, detailed investigation of the structural relaxation energy, effective electron/hole mass, and size-scaling of the bandgap as a function of size and chirality using accurate screened-exchange DFT calculations. These calculations provide a systematic evaluation of the structural and electronic properties of the largest graphdiyne nanotubes to date, up to 1296 atoms and 23328 basis functions. Furthermore, these large-scale calculations allow us to present simple analytical formulas to guide future experimental efforts for estimating the fundamental bandgaps of these unique nanotubes as a function of chirality and diameter as well as provide a detailed understanding of the size-scaling of structural and electronic properties. Finally, we give a detailed analysis of all these effects for both the armchair and zigzag GDNTs and discuss the implications of these computed properties on electron/hole mobility and potential applications of these results.

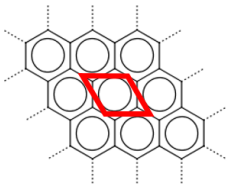

graphene

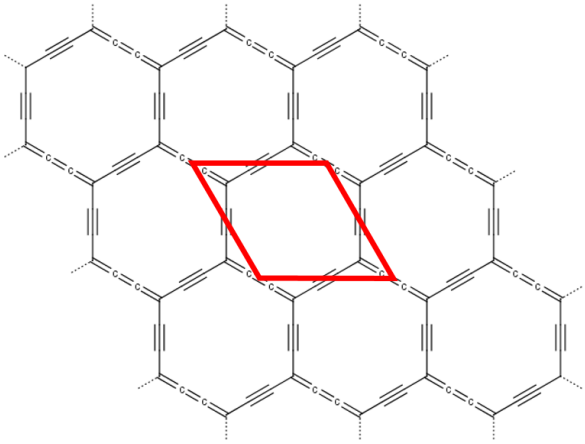

α-graphyne

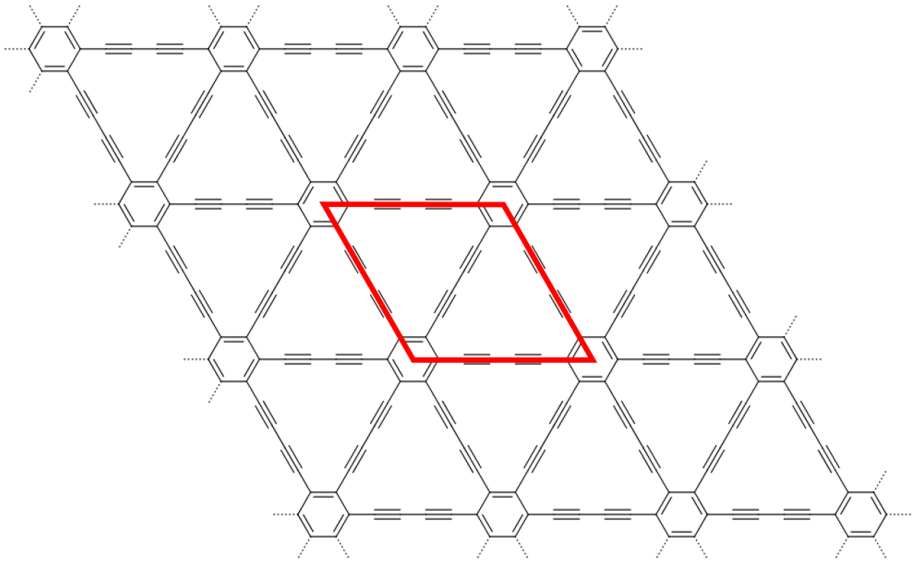

graphdiyne

Figure 1.1. Chemical structures and unit cells for graphene, α-graphyne, and graphdiyne. All structures and unit cells are drawn to scale, with each unit cell containing 2, 8, and 18 carbon atoms for graphene, α-graphyne, and graphdiyne, respectively.

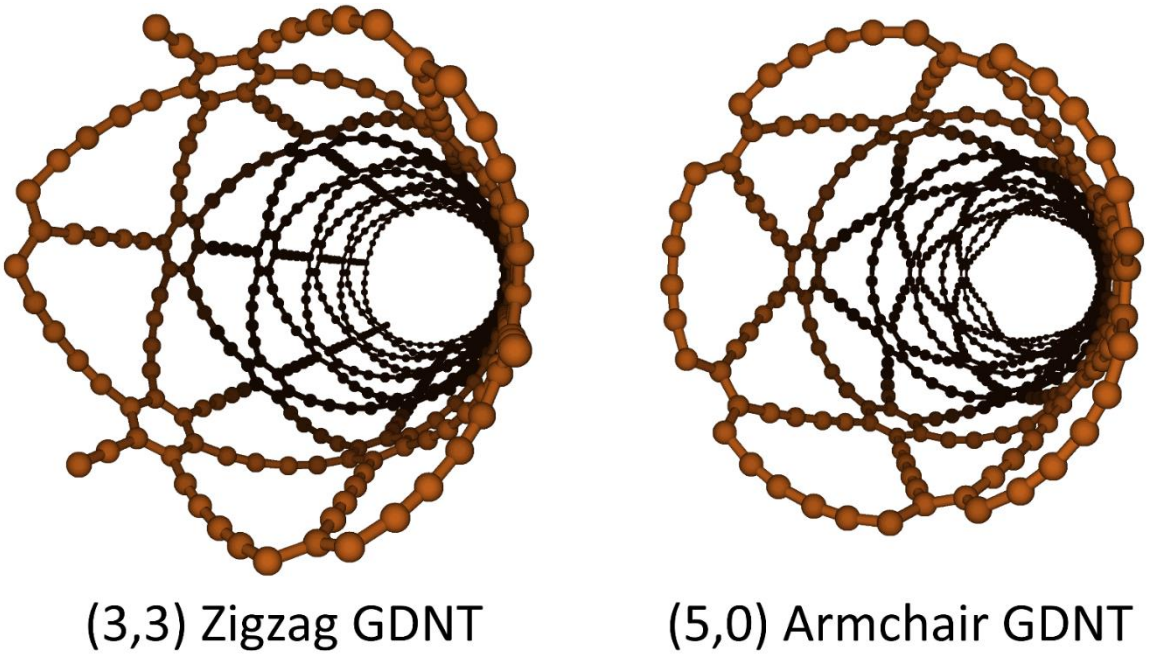

Figure 1.2. Optimized structures of the (3,3) zigzag and (5,0) armchair graphdiyne nanotubes.

II. Structural Properties of Graphdiyne Nanotubes

Planar graphdiyne belongs to the *p6mm* space group, and its unit cell is defined by the two lattice vectors $\vec{a}_1 = a\hat{x}$ and $\vec{a}_2 = \frac{a}{2}\left(-\hat{x} + \sqrt{3}y\right)$, as shown in Figure 1.3. Any GDNT of arbitrary chirality can be generated by these two vectors through the chiral vector $\vec{C}_h = n\vec{a}_1 - m\vec{a}_2$, where $\left|\vec{C}_h\right| = ac_h$, $\left[c_h \equiv (n^2 + m^2 + nm)^{1/2}\right]$, and the tube diameter is given by $d_t = \frac{ac_h}{\pi}$. The chiral angle, as shown in Figure 1.3, is defined by $\cos\theta = \frac{2n+m}{2c_h}$, where $0 \leq \theta \leq \pi/6$. Based on these definitions for the chiral vector and chiral angle, armchair GDNTs $(\theta = 0)$ are represented by the (n, 0) chiral index, and zigzag GDNTs $(\theta = \pi/6)$ are characterized by the (n, n) chiral index, *which is the*

opposite convention in carbon nanotubes. Figure 1.3 illustrates the lattice vectors and selected examples of chiral vectors for a (3, 0) armchair and (2, 2) zigzag GDNT.

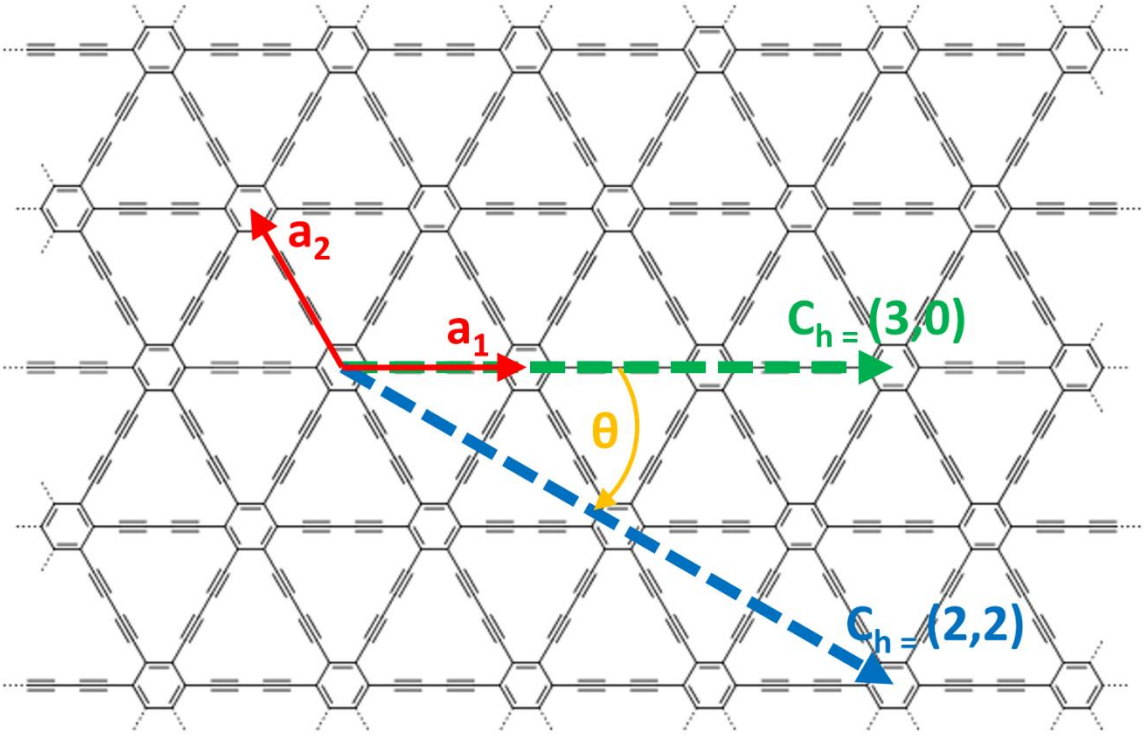

Figure 1.3. Lattice vectors $\vec{a}_1$ and $\vec{a}_2$, chiral angle θ, and selected chiral vectors (3,0) and (2,2) for a graphydiyne sheet.

III. Theory and Methodology

All calculations were carried out with a massively parallelized version of the CRYSTAL14 program,[21] which has the capability of using both all-electron Gaussian-type orbitals and exact Hartree–Fock exchange within periodic boundary conditions. The latter is particularly important for obtaining accurate electronic properties for periodic systems since the incorporation of Hartree–Fock exchange can partially correct for electron-delocalization errors inherent to both LDA (local density approximation) and GGA (generalized gradient approximation) exchange-correlation functionals. For this

reason, we utilized the range-separated HSE06 functional[22] for obtaining the electronic properties for both the graphdiyne sheet and all of the zigzag and armchair graphdiyne nanotubes. As opposed to range-separated hybrid DFT methods that incorporate a "full" range separation of 100% asymptotic Hartree–Fock exchange (typically used in isolated molecules[23-28]), the HSE06 functional incorporates a screened Hartree–Fock exchange that decays to zero. Most importantly, our previous studies[29] with the HSE06 functional in the CRYSTLA14 program has shown that it is much more computationally efficient than conventional global hybrid functionals[30] and is significantly more accurate than conventional semilocal functionals. It is worth noting that, although the HSE06 calculations are more efficient than conventional hybrid DFT methods, the calculations on some of the largest GDNTs were still extremely computationally intensive due to the immense size of these nanotubes. For example, the largest of these structures (specifically the (36,0) armchair GDNT), consists of 1296 atoms and 23328 basis functions and, as such, this study constitutes the largest systematic study of these nanostructures to date.

Geometries for all of the graphydiyne nanotubes were optimized using a large TZVP all-electron basis set[31] with one-dimensional periodic boundary conditions along the tube axis. At the optimized geometries, a final single-point HSE06 calculation was performed with 100 k-points along the one-dimensional Brillouin zone to obtain the electronic band structure for all of the nanotube geometries.

IV. Results and Discussion

A. Benchmark Calculations

Since a systematic study of the electronic properties of armchair and zigzag GDNTs has not been previously investigated, we first benchmarked our HSE06/TZVP results for the graphdiyne sheet against the high-level G0W0 (Green's function G and screened Coulomb interaction W) calculations by Luo et al.[32] In this previous study, the G0W0 bandgap of the planar graphdiyne sheet attains a value of 1.10 eV, which is consistent with experimental measurements of graphdiyne film. The band structure along high-symmetry points in the graphdiyne Brillouin zone (defined by the high-symmetry points Γ, X, and M in momentum space) obtained by our HSE06/TZVP calculations is shown in Figure 1.4. We obtain a direct bandgap of 1.26 eV at the Γ point, which is in relatively good agreement with the computationally intensive G0W0 bandgap of 1.10 eV. The close agreement between our HSE06 results is in stark contrast to conventional PBE calculations, which severely underestimate the bandgap by more than 50%, giving a value of 0.54 eV. As such, our benchmark calculations for the bandgap of planar graphdiyne demonstrate that our HSE06 calculations are reasonable for our parametric studies on the various GDNTs studied in this work.

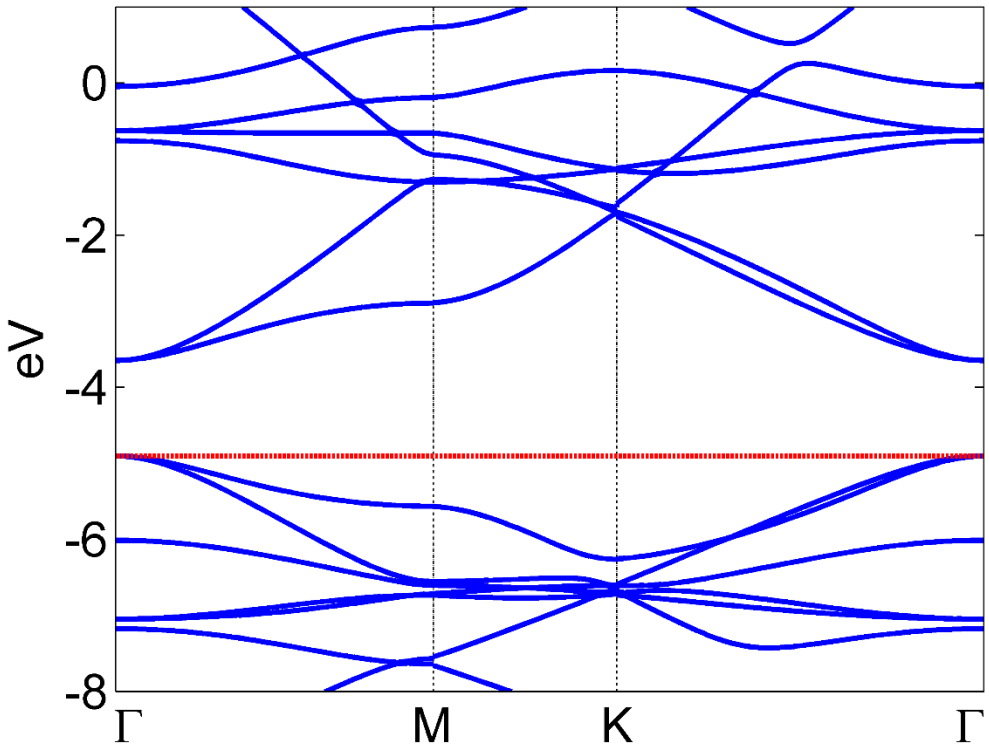

Figure 1.4. Electronic band structure for planar graphdiyne obtained at the HSE06/TZVP level of theory. The dashed horizontal line indicates the position of the Fermi energy, and a direct bandgap of 1.26 eV occurs at the Γ point within the irreducible Brillouin zone.

B. Structural Properties

To give deeper insight into the structural stability of all the nanotubes relative to the planar graphdiyne sheet, we calculated the relaxation energy, ΔE, given by

$$\Delta E = E_{\text{nanotube}} - n \cdot E_{\text{sheet}} \quad (1)$$

where E_{nanotube} is the electronic energy of the geometry-optimized nanotube, E_{sheet} is the electronic energy of the graphdiyne sheet, and n is the number of repeat units along the nanotube circumference (which also corresponds to the first chiral index for each (n,m) nanotube). Figure 1.5 shows that ΔE decreases monotonically with size, and the stability

becomes comparable to planar graphdiyne for GDNT diameters larger than 9 nm. To further test the structural stability of these nanostructures, we calculated the harmonic frequencies for the smallest (2,2) GDNT, which contains 72 atoms in its primitive unit cell (harmonic frequency calculations for other larger GDNTs were computationally out of reach due to their immense size; for example, the largest GDNT in this work contains up to 1296 atoms and 23328 basis functions). At the optimized geometry, we obtained real-valued frequencies for all of the vibrational modes for the (2,2) GDNT (vibrational frequencies, symmetries, and infrared/Raman analysis for the (2,2) GDNT can be found in the Appendix) . Most importantly, since the (2,2) GDNT is the most strained nanotube in this study (cf. Figure 1.5), our stability analysis also implies that the other larger, less-strained GDNTs are also structurally stable. We also tabulated the binding energy per atom for all GDNTs in Tables 1.1 and 1.2 using the expression

$$E_{binding} = \frac{1}{N}\left(E_{\text{nanotube}} - N \cdot E_{atom}\right) \quad (2)$$

where N is the number of atoms in the nanotube, E_{nanotube} is the electronic energy of the geometry-optimized nanotube, and E_{atom} is the total atomic energy of the carbon atom (in its ground triplet state). Similar to the computed relaxation energies, the binding energy per atom decreases monotonically with diameter and becomes nearly constant for GDNT diameters larger than 9 nm. To compare the structural stabilities of these GDNTs against conventional nanostructures, we also calculated the binding energy per atom for a conventional (13,0) carbon nanotube, which has a similar diameter to a (2,2) zigzag GDNT. At the HSE06/TZVP level of theory, we obtain a binding energy per atom of −7.9480 eV, which is 0.88 eV more stable than a similarly sized (2,2) zigzag GDNT. It is

also interesting to note that the zigzag GDNTs are structurally more stable compared to armchair GDNTs of the same size. This trend can be rationalized since the geometric structures of the armchair and zigzag GDNTs are topologically different. Specifically, all six of the acetylenic linkages (between the benzene rings) in armchair GDNTs straddle the circumference of the nanotube, whereas two of the acetylenic linkages in the zigzag GDNTs are oriented along the nanotube axis (cf. Figure 1.2), which partially relieves these strain effects around the GDNT circumference.

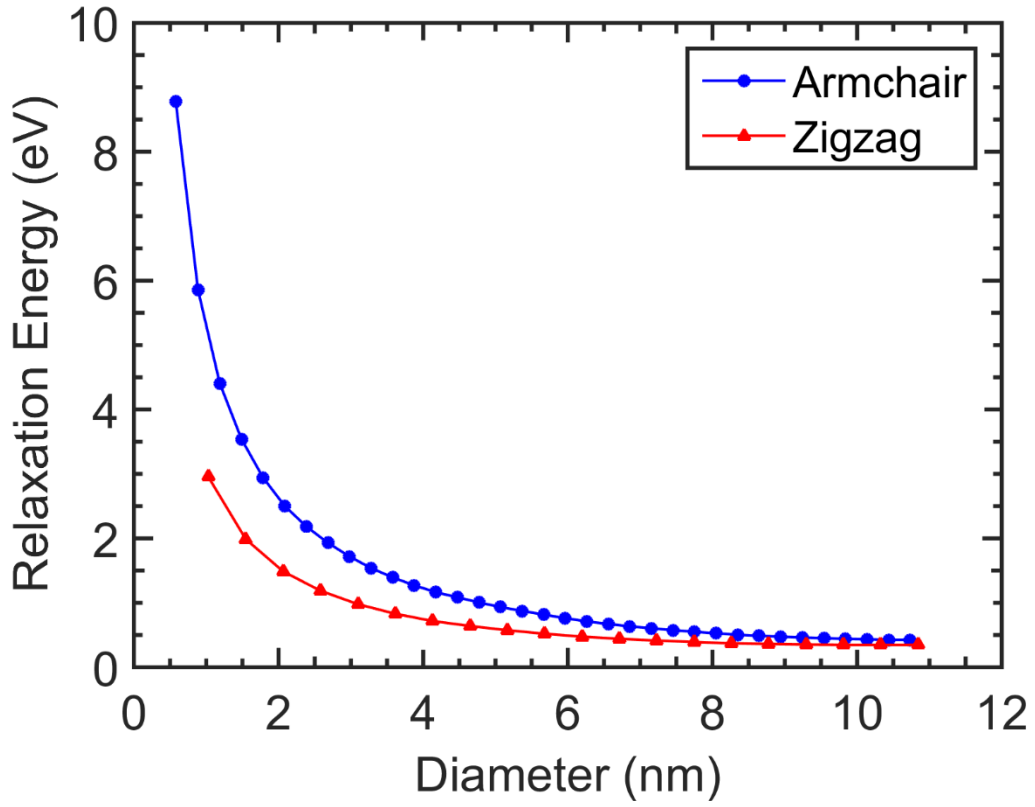

Figure 1.5. Relaxation energy, ΔE, as a function of diameter for both armchair and zigzag GDNTs obtained at the HSE06/TZVP level of theory.

C. Electronic Properties

Figures 1.6 and 1.7 plot the band structures of selected armchair and zigzag GDNTs, respectively, along the irreducible Brillouin zone (defined by the high-symmetry points Γ and X in momentum space). In all of the different chiralities, we find that the electronic band structures are characterized by a direct bandgap at the Γ point. We calculated the effective mass m^* of the electrons and holes at the conduction band minimum and valence band maximum, respectively, using the expression

$$m = \pm\hbar^2 \left(\frac{d^2E}{dk^2}\right)^{-1}. \quad (3)$$

The positive sign is taken for the (electron) conduction band, and the negative sign corresponds to the (hole) valence band. Tables 1.1 and 1.2 give a summary of the various structural and electronic properties (radii, relaxation energies, binding energy per atom, effective electron mass, effective hole mass, and bandgaps) of the armchair and zigzag GDNTs examined in this study

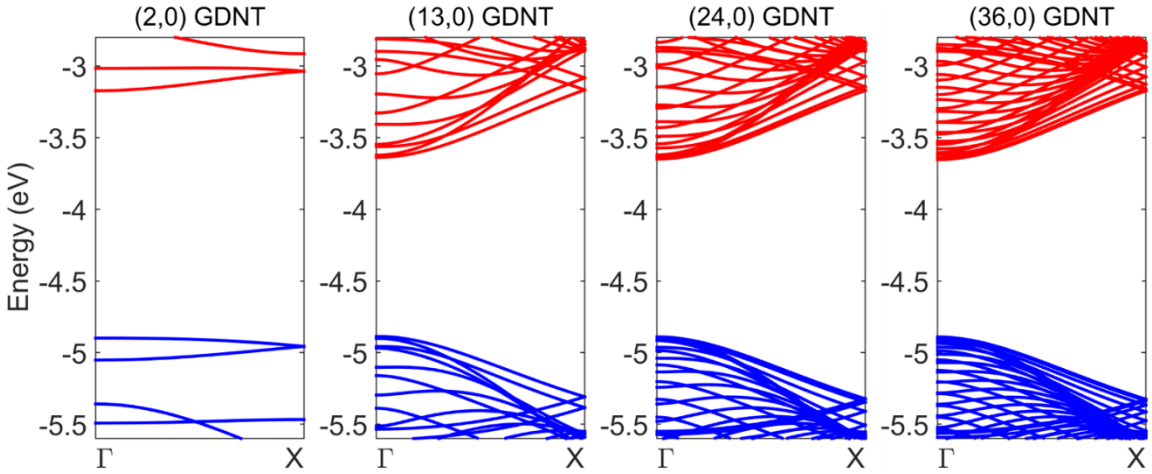

Figure 1.6. Electronic band structures (relative to vacuum at 0 eV) of various (n,0) armchair GDNTs for n = 2, 13, 24, and 36. Note the narrow (and nearly dispersionless) bands for the (2,0) GDNT.

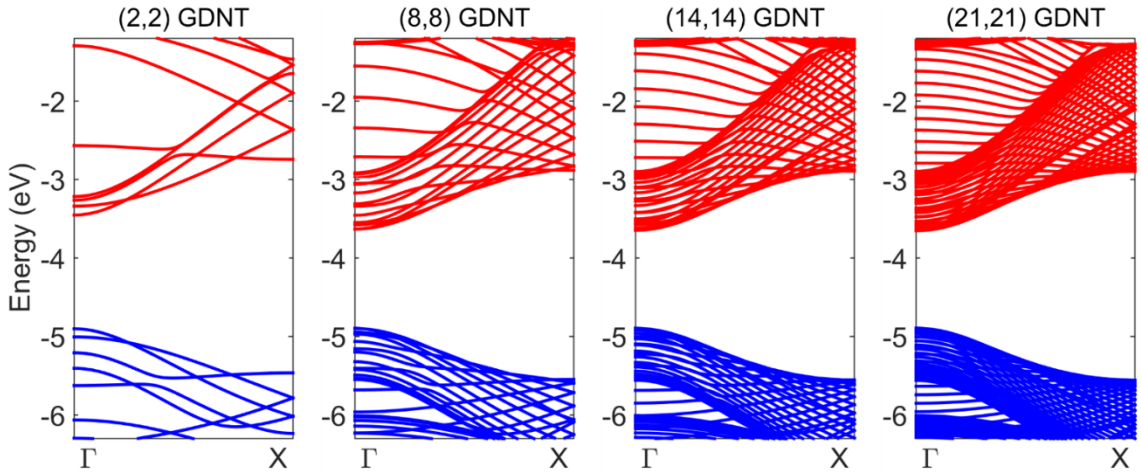

Figure 1.7. Electronic band structures (relative to vacuum at 0 eV) of various (n,n) zigzag GDNTs for n = 2, 8, 14, and 21. Note that the zigzag GDNTs have wider valence and conduction bands compared to their armchair GDNT counterparts.

Table 1.1. Radii, Relaxation Energies, Binding Energies per Atom, Effective Electron Mass, Effective Hole Mass, and Bandgaps of Armchair Graphdiyne Nanotubes

Subunits	Radius (nm)	Relaxation Energy (eV)	Binding Energy per atom (eV)	Electron Mass (m_e)	Hole Mass (m_e)	Bandgap (eV)
2	0.29	8.78	–6.9866	0.518	4.451	1.727
3	0.44	5.86	–7.0543	0.256	0.412	1.433
4	0.59	4.41	–7.0780	0.207	0.271	1.339
5	0.74	3.54	–7.0890	0.187	0.227	1.300
6	0.89	2.94	–7.0949	0.178	0.206	1.281
7	1.04	2.50	–7.0986	0.172	0.195	1.270
8	1.19	2.19	–7.1010	0.168	0.188	1.263
9	1.34	1.93	–7.1026	0.166	0.183	1.258
10	1.49	1.72	–7.1038	0.164	0.18	1.255
11	1.64	1.54	–7.1047	0.163	0.177	1.252
12	1.79	1.39	–7.1053	0.162	0.175	1.251
13	1.94	1.27	–7.1059	0.161	0.174	1.249
14	2.09	1.16	–7.1063	0.161	0.173	1.248
15	2.24	1.09	–7.1066	0.16	0.172	1.247
16	2.38	1.01	–7.1068	0.16	0.171	1.246
17	2.53	0.93	–7.1070	0.16	0.171	1.245
18	2.68	0.87	–7.1072	0.159	0.17	1.245
19	2.83	0.82	–7.1074	0.159	0.17	1.244
20	2.98	0.76	–7.1075	0.159	0.17	1.244
21	3.13	0.71	–7.1076	0.159	0.169	1.243
22	3.28	0.67	–7.1077	0.158	0.169	1.243
23	3.43	0.63	–7.1078	0.158	0.169	1.242
24	3.58	0.60	–7.1079	0.158	0.168	1.242
25	3.73	0.58	–7.1079	0.158	0.168	1.242
26	3.88	0.55	–7.1080	0.158	0.168	1.241
27	4.02	0.53	–7.1080	0.158	0.168	1.241
28	4.17	0.50	–7.1081	0.158	0.168	1.241
29	4.32	0.49	–7.1081	0.158	0.168	1.241
30	4.47	0.47	–7.1081	0.158	0.168	1.240
31	4.62	0.46	–7.1082	0.158	0.167	1.240
32	4.77	0.45	–7.1082	0.158	0.167	1.240
33	4.92	0.44	–7.1082	0.157	0.167	1.240
34	5.07	0.43	–7.1082	0.157	0.167	1.239
35	5.22	0.43	–7.1082	0.157	0.167	1.239
36	5.37	0.43	–7.1082	0.157	0.167	1.239

Table 1.2. Radii, Relaxation Energies, Binding Energies Per Atom, Effective Electron Mass, Effective Hole Mass, and Bandgaps of Zigzag Graphdiyne Nanotubes

Subunits	Radius (nm)	Relaxation Energy (eV)	Binding Energy per atom (eV)	Electron Mass (m_e)	Hole Mass (m_e)	Bandgap (eV)
2	0.51	2.95	–7.0675	0.191	0.215	1.450
3	0.77	1.99	–7.0902	0.163	0.171	1.344
4	1.03	1.49	–7.0982	0.161	0.172	1.303
5	1.29	1.19	–7.1020	0.169	0.18	1.285
6	1.55	0.98	–7.1040	0.160	0.171	1.274
7	1.81	0.83	–7.1053	0.163	0.174	1.268
8	2.07	0.72	–7.1061	0.159	0.17	1.264
9	2.32	0.64	–7.1066	0.160	0.171	1.261
10	2.58	0.57	–7.1070	0.158	0.169	1.257
11	2.84	0.52	–7.1073	0.159	0.17	1.255
12	3.1	0.47	–7.1075	0.158	0.168	1.252
13	3.36	0.44	–7.1076	0.158	0.169	1.250
14	3.61	0.41	–7.1077	0.157	0.168	1.249
15	3.87	0.39	–7.1078	0.158	0.168	1.247
16	4.13	0.37	–7.1079	0.157	0.168	1.246
17	4.39	0.36	–7.1080	0.157	0.168	1.245
18	4.65	0.35	–7.1080	0.157	0.167	1.244
19	4.91	0.35	–7.1081	0.157	0.168	1.243
20	5.16	0.35	–7.1081	0.157	0.167	1.242
21	5.42	0.35	–7.1081	0.157	0.167	1.242

Figure 1.8 plots the bandgap of the armchair and zigzag GDNTs as a function of nanotube radius. Using our HSE06/TZVP calculations, we performed a nonlinear fit of the bandgap (E_g) as a function of diameter (d). We chose a flexible functional form given by $E_g = A/d + B$, where A and B are independent free parameters subject to our nonlinear least-squares fit. Based on our HSE06 bandgaps, we obtained fitted expressions

$$E_g(\text{armchair}) = \frac{0.24\ \text{eV}}{d\ (\text{in nm})} + 1.2\ \text{eV} \quad (4)$$

$$E_g(\text{zigzag}) = \frac{0.21\ \text{eV}}{d\ (\text{in nm})} + 1.2\ \text{eV} \quad (5)$$

with R-squared fit values of 0.87 and 0.97, respectively (the slightly lower R-squared fit value for the armchair GDNTs arises from larger strain values compared to their zigzag GDNTs counterparts [cf. Figure 1.5]). It is interesting to note that the last constant term in Equations (4) and (5) corresponds closely to the bandgap of the planar graphdiyne sheet; in other words, the constant term in Equations (4) and (5) yields the bandgap of a GDNT having an infinite diameter. Although we determined this constant as a free parameter in our fit, it is noteworthy to point out that we nearly recover the bandgap of planar graphdiyne calculated earlier in Section IV.A (we do not obtain the exact bandgap of planar graphdiyne due to relatively strong curvature effects that are still present in the larger GDNTs).

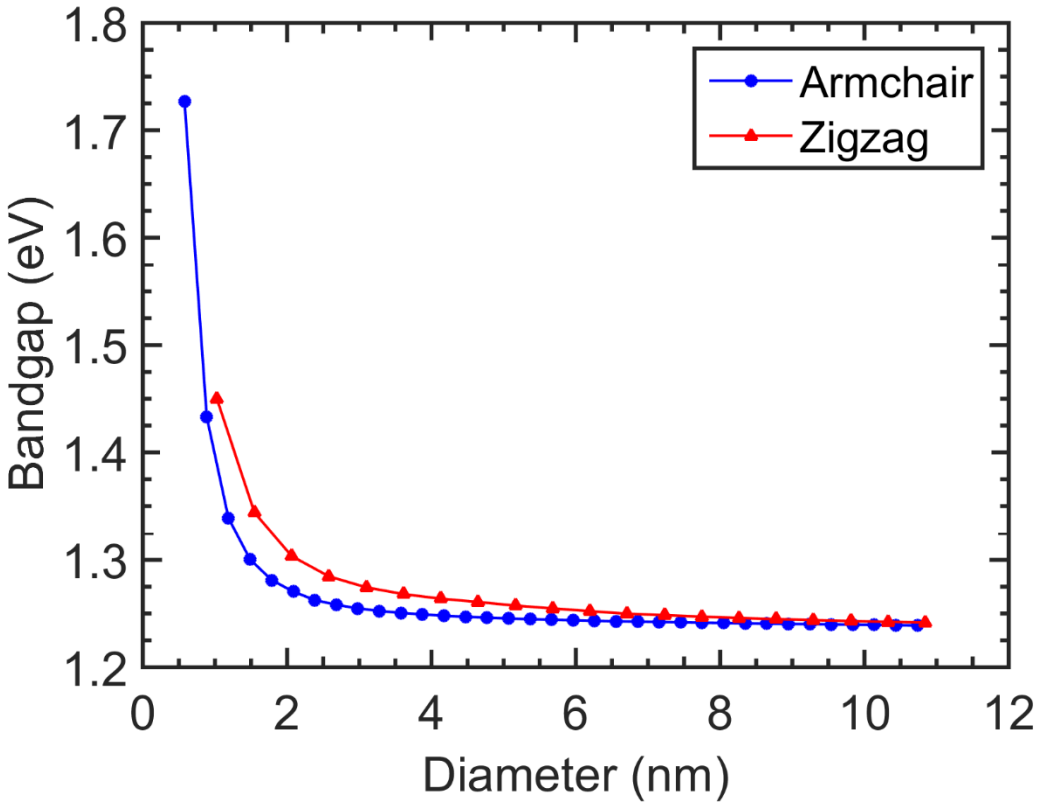

Figure 1.8. Electronic bandgap as a function of diameter for both armchair and zigzag GDNTs obtained at the HSE06/TZVP level of theory.

Finally, we examine in greater detail the electronic band structures of both the armchair and zigzag GDNTs. As shown in Figures 1.6 and 1.7, the armchair GDNTs possess narrower valence and conduction bands, whereas the zigzag GDNTs exhibit much wider bands (band structures for all 35 armchair and all 20 zigzag GDNTs can be found in the Appendix). Specifically, the width of an electronic band reflects the orbital interactions along the nanotube axis, with wide bands denoting orbital delocalization and narrow bands corresponding to localization (small overlap). To corroborate these findings, we plotted the highest occupied crystal orbital (HOCO) and lowest unoccupied crystal orbital (LUCO) at the Γ point for both the armchair and zigzag GDNTs (using the

same isosurface values for each). Figure 1.9 shows that both the HOCO and LUCO in armchair GDNTs are localized on the acetylenic linkages along the circumference of the nanotube. In contrast, for zigzag GDNTs, the HOCO and LUCO are delocalized along the entire axis of zigzag and, therefore, both hole- and electron-transport are more facile in zigzag GDNTs compared to their armchair counterparts. While the bandgaps for both the armchair and zigzag GDNTs can certainly be tuned as a function of size, the conductivity in each of these two different chiralities is markedly different. Zigzag GDNTs have wider valence and conduction bands (which are demonstrated by the orbital diagrams in Figure 1.9 and the projected density of states plots in Figure 1.10) and are, therefore, expected to have a higher conductivity than their armchair counterparts. As such, both the armchair and the zigzag chiralities provide an additional intrinsic material property that can be used to modulate both hole- and electron-transport in photoinduced applications and processes.

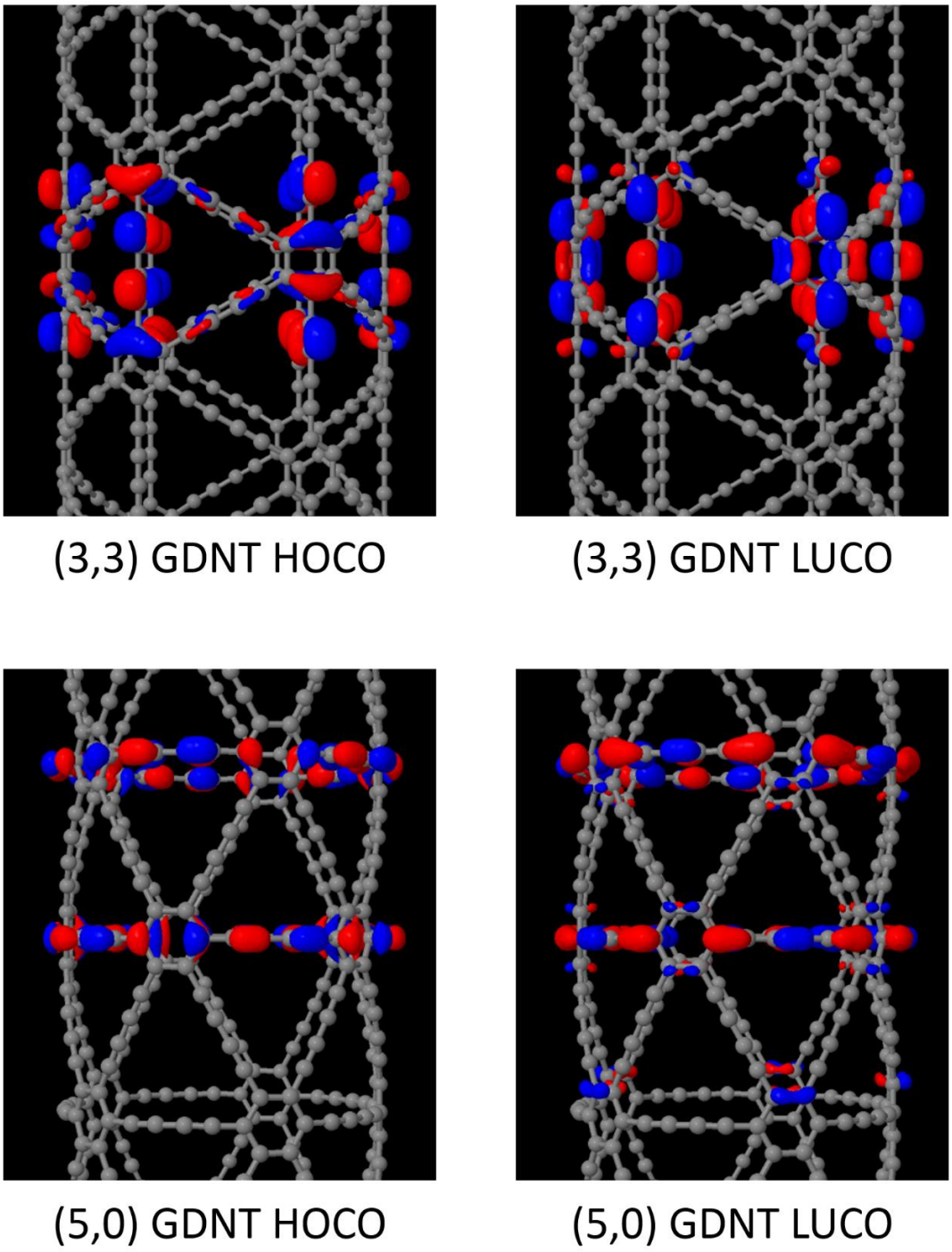

Figure 1.9. Highest occupied and lowest unoccupied crystal orbitals (HOCO and LUCO) for the (5,0) armchair and (3,3) zigzag GDNTs (only crystal orbitals within one unit cell are shown for clarity). Both the HOCO and LUCO are localized along acetylenic linkages along the circumference of the (5,0) GDNT, whereas the HOCO and LUCO are localized along acetylenic linkages along the axis of the (3,3) GDNT.

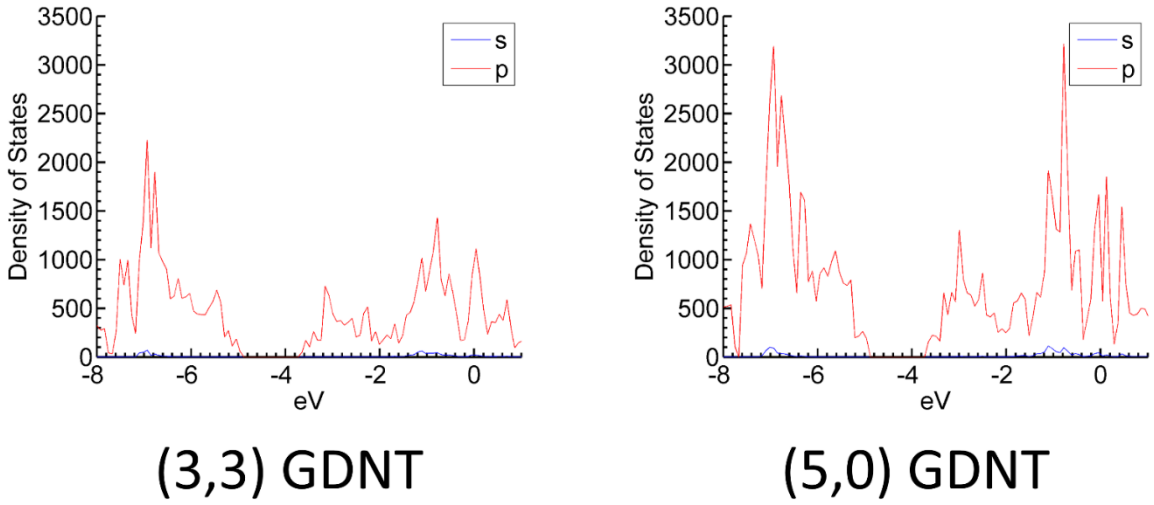

Figure 1.10. Projected density of states for the (3,3) zigzag and (5,0) armchair GDNT. For both the (3,3) and (5,0) GDNT, the carbon p orbitals contribute a significant fraction of the total density of states.

V. Conclusion

Within this extensive theoretical study, we have systematically calculated the structural and electronic properties in a series of armchair and zigzag graphdiyne nanotubes via large-scale DFT calculations. Our calculations utilize the HSE06 functional (which gives accurate estimates of the bandgap compared to computationally expensive G0W0 calculations), and we present quantitative predictions of the structural relaxation energy, effective electron/hole mass, and size-scaling of the bandgap as a function of size and chirality. These calculations provide a systematic evaluation of the structural and electronic properties of the largest graphdiyne nanotubes to date (up to 1,296 atoms and 23,328 basis functions). To the best of our knowledge, a systematic study on the structural and electronic properties of GDNTs as a function of size and chirality has not been previously reported. Our calculations find that zigzag GDNTs are

structurally more stable compared to armchair GDNTs of the same size. Furthermore, these large-scale calculations allow us to present simple analytical formulas to guide future experimental efforts for estimating the fundamental bandgaps of these unique nanotubes as a function of chirality and diameter. While the bandgaps for both the armchair and zigzag GDNTs can be tuned as a function of size, the conductivity in each of these two different chiralities is markedly different. Both the HOCO and LUCO in armchair GDNTs are localized on the acetylenic linkages along the circumference of the nanotube. In contrast, the HOCO and LUCO are delocalized along the entire axis of zigzag GDNTs and, therefore, both hole- and electron-transport are more facile in zigzag GDNTs compared to their armchair counterparts.

Looking forward, it would be of immense interest to understand and predict the excited-state and optoelectronic properties of these GDNTs using first-principles theoretical methods. As planar graphdiyne has garnered very recent attention as a photocatalyst for hydrogen production,[17] the use of GDNTs would offer additional electronic properties that can be tailored for these photoelectrochemical processes. For example, the bandgaps of both the armchair and zigzag GDNTs can be tuned as a function of diameter and, therefore, can be used as photoabsorbers that span a wide range of the solar spectrum. Furthermore, since both hole- and electron-transport are qualitatively different in armchair and zigzag GDNTs, these nanomaterials provide a new opportunity for modulating both charge- and energy-transfer dynamics in these photocatalytic systems.

VI. References

1. Iijima, S., Helical microtubules of graphitic carbon. *Nature* **1991,** *354*, 56-58.

2. Hu, J.; Odom, T. W.; Lieber, C. M., Chemistry and Physics in One Dimension: Synthesis and Properties of Nanowires and Nanotubes. *Accounts of Chemical Research* **1999,** *32*, 435-445.

3. Zhou, X. J.; Zifer, T.; Wong, B. M.; Krafcik, K. L.; Leonard, F.; Vance, A. L., Color Detection Using Chromophore-Nanotube Hybrid Devices. *Nano Lett* **2009,** *9*, 1028-1033.

4. Wong, B. M.; Morales, A. M., Enhanced photocurrent efficiency of a carbon nanotube p-n junction electromagnetically coupled to a photonic structure. *J Phys D Appl Phys* **2009,** *42*.

5. Zhao, Y. C.; Huang, C. S.; Kim, M.; Wong, B. M.; Leonard, F.; Gopalan, P.; Eriksson, M. A., Functionalization of Single-Wall Carbon Nanotubes with Chromophores of Opposite Internal Dipole Orientation. *Acs Appl Mater Inter* **2013,** *5*, 9355-9361.

6. Joo, Y.; Brady, G. J.; Shea, M. J.; Oviedo, M. B.; Kanimozhi, C.; Schmitt, S. K.; Wong, B. M.; Arnold, M. S.; Gopalan, P., Isolation of Pristine Electronics Grade Semiconducting Carbon Nanotubes by Switching the Rigidity of the Wrapping Polymer Backbone on Demand. *ACS Nano* **2015,** *9*, 10203-10213.

7. Ford, A. C.; Shaughnessy, M.; Wong, B. M.; Kane, A. A.; Kuznetsov, O. V.; Krafcik, K. L.; Billups, W. E.; Hauge, R. H.; Leonard, F., Physical removal of metallic carbon nanotubes from nanotube network devices using a thermal and fluidic process. *Nanotechnology* **2013,** *24*.

8. Huang, C. S.; Wang, R. K.; Wong, B. M.; Mcgee, D. J.; Leonard, F.; Kim, Y. J.; Johnson, K. F.; Arnold, M. S.; Eriksson, M. A.; Gopalan, P., Spectroscopic Properties of Nanotube-Chromophore Hybrids. *Acs Nano* **2011,** *5*, 7767-7774.

9. Spinks, G. M.; Wallace, G. G.; Fifield, L. S.; Dalton, L. R.; Mazzoldi, A.; De Rossi, D.; Khayrullin, I. I.; Baughman, R. H., Pneumatic Carbon Nanotube Actuators. *Advanced Materials* **2002,** *14*, 1728-1732.

10. Vohrer, U.; Kolaric, I.; Haque, M. H.; Roth, S.; Detlaff-Weglikowska, U., Carbon nanotube sheets for the use as artificial muscles. *Carbon* **2004,** *42*, 1159-1164.

11. Simmons, T. J.; Hashim, D.; Vajtai, R.; Ajayan, P. M., Large Area-Aligned Arrays from Direct Deposition of Single-Wall Carbon Nanotube Inks. *Journal of the American Chemical Society* **2007,** *129*, 10088-10089.

12. Guldi, D. M.; Rahman, G. M. A.; Prato, M.; Jux, N.; Qin, S.; Ford, W., Single-Wall Carbon Nanotubes as Integrative Building Blocks for Solar-Energy Conversion. *Angewandte Chemie* **2005,** *117*, 2051-2054.

13. Wilder, J. W. G.; Venema, L. C.; Rinzler, A. G.; Smalley, R. E.; Dekker, C., Electronic structure of atomically resolved carbon nanotubes. *Nature* **1998,** *391*, 59-62.

14. Shao, Z.-G.; Ye, X.-S.; Yang, L.; Wang, C.-L., First-principles calculation of intrinsic carrier mobility of silicene. *Journal of Applied Physics* **2013,** *114*, 093712.

15. Cranford, S. W.; Buehler, M. J., Selective hydrogen purification through graphdiyne under ambient temperature and pressure. *Nanoscale* **2012,** *4*, 4587-4593.

16. Jalili, S.; Houshmand, F.; Schofield, J., Study of carrier mobility of tubular and planar graphdiyne. *Applied Physics a-Materials Science & Processing* **2015,** *119*, 571-579.

17. Li, J.; Gao, X.; Liu, B.; Feng, Q.; Li, X.-B.; Huang, M.-Y.; Liu, Z.; Zhang, J.; Tung, C.-H.; Wu, L.-Z., Graphdiyne: A Metal-Free Material as Hole Transfer Layer To Fabricate Quantum Dot-Sensitized Photocathodes for Hydrogen Production. *Journal of the American Chemical Society* **2016,** *138*, 3954-3957.

18. Jiao, Y.; Du, A. J.; Hankel, M.; Zhu, Z. H.; Rudolph, V.; Smith, S. C., Graphdiyne: a versatile nanomaterial for electronics and hydrogen purification. *Chemical Communications* **2011,** *47*, 11843-11845.

19. Li, G.; Li, Y.; Qian, X.; Liu, H.; Lin, H.; Chen, N.; Li, Y., Construction of Tubular Molecule Aggregations of Graphdiyne for Highly Efficient Field Emission. *The Journal of Physical Chemistry C* **2011,** *115*, 2611-2615.

20. Long, M.; Tang, L.; Wang, D.; Li, Y.; Shuai, Z., Electronic Structure and Carrier Mobility in Graphdiyne Sheet and Nanoribbons: Theoretical Predictions. *ACS Nano* **2011,** *5*, 2593-2600.

21. Dovesi, R.; Orlando, R.; Erba, A.; Zicovich-Wilson, C. M.; Civalleri, B.; Casassa, S.; Maschio, L.; Ferrabone, M.; De La Pierre, M.; D'Arco, P.; Noël, Y.; Causà, M.; Rérat, M.; Kirtman, B., CRYSTAL14: A program for the ab initio investigation of crystalline solids. *International Journal of Quantum Chemistry* **2014,** *114*, 1287-1317.

22. Heyd, J.; Scuseria, G. E., Efficient hybrid density functional calculations in solids: Assessment of the Heyd–Scuseria–Ernzerhof screened Coulomb hybrid functional. *The Journal of Chemical Physics* **2004,** *121*, 1187-1192.

23. Raeber, A. E.; Wong, B. M., The Importance of Short- and Long-Range Exchange on Various Excited State Properties of DNA Monomers, Stacked Complexes, and Watson–Crick Pairs. *Journal of Chemical Theory and Computation* **2015,** *11*, 2199-2209.

24. Katan, C.; Savel, P.; Wong, B. M.; Roisnel, T.; Dorcet, V.; Fillaut, J. L.; Jacquemin, D., Absorption and fluorescence signatures of 1,2,3-triazole based regioisomers: challenging compounds for TD-DFT. *Phys Chem Chem Phys* **2014,** *16*, 9064-9073.

25. Foster, M. E.; Wong, B. M., Nonempirically Tuned Range-Separated DFT Accurately Predicts Both Fundamental and Excitation Gaps in DNA and RNA Nucleobases. *Journal of Chemical Theory and Computation* **2012,** *8*, 2682-2687.

26. Wong, B. M.; Hsieh, T. H., Optoelectronic and Excitonic Properties of Oligoacenes: Substantial Improvements from Range-Separated Time-Dependent Density Functional Theory. *Journal of Chemical Theory and Computation* **2010,** *6*, 3704-3712.

27. Wong, B. M.; Piacenza, M.; Della Sala, F., Absorption and fluorescence properties of oligothiophene biomarkers from long-range-corrected time-dependent density functional theory. *Phys Chem Chem Phys* **2009,** *11*, 4498-4508.

28. Wong, B. M.; Cordaro, J. G., Coumarin dyes for dye-sensitized solar cells: A long-range-corrected density functional study. *Journal of Chemical Physics* **2008,** *129*.

29. Allec, S. I.; Ilawe, N. V.; Wong, B. M., Unusual Bandgap Oscillations in Template-Directed π-Conjugated Porphyrin Nanotubes. *The Journal of Physical Chemistry Letters* **2016,** *7*, 2362-2367.

30. Wong, B. M.; Ye, S. H., Self-assembled cyclic oligothiophene nanotubes: Electronic properties from a dispersion-corrected hybrid functional. *Physical Review B* **2011,** *84*.

31. Peintinger, M. F.; Oliveira, D. V.; Bredow, T., Consistent Gaussian basis sets of triple-zeta valence with polarization quality for solid-state calculations. *Journal of Computational Chemistry* **2013,** *34*, 451-459.

32. Guangfu, L.; Xuemin, Q.; Huibiao, L.; Rui, Q.; Jing, Z.; Linze, L.; Zhengxiang, G.; Enge, W.; Wai-Ning, M.; Jing, L.; Yuliang, L.; Nagase, S., Quasiparticle energies and excitonic effects of the two-dimensional carbon allotrope graphdiyne: Theory and experiment. *Physical Review B (Condensed Matter and Materials Physics)* **2011,** *84*, 075439 (5 pp.)-075439 (5 pp.).

Sulfate Radical Oxidation of Aromatic Contaminants: A Detailed Assessment of Density Functional Theory and High-Level Quantum Chemical Methods

Abstract. Advanced oxidation processes that utilize highly oxidative radicals are widely used in water reuse treatment. In recent years, the application of sulfate radical ($SO_4^{\bullet-}$) as a promising oxidant for water treatment has gained increasing attention. To understand the efficiency of $SO_4^{\bullet-}$ in the degradation of organic contaminants in wastewater effluent, it is important to be able to predict the reaction kinetics of various $SO_4^{\bullet-}$-driven oxidation reactions. In this study, we utilize density functional theory (DFT) and high-level wavefunction-based methods (including computationally-intensive coupled cluster methods), to explore the activation energies and kinetic rates of $SO_4^{\bullet-}$-driven oxidation reactions on a series of benzene-derived contaminants. These high-level calculations encompassed a wide set of reactions including 110 forward/reverse reactions and 5 different computational methods in total. Based on the high-level coupled-cluster quantum calculations, we find that the popular M06-2X DFT functional is significantly more accurate for OH^- additions than for $SO_4^{\bullet-}$ reactions. Most importantly, we highlight some of the limitations and deficiencies of other computational methods, and we

recommend the use of high-level quantum calculations to spot-check environmental chemistry reactions that may lie outside the training set of the M06-2X functional, particularly for water oxidation reactions that involve $SO_4^{\bullet-}$ and other inorganic species.

I. Introduction

Water scarcity has become a global crisis. This situation is exacerbated – and will continue to be dominated – by the global shrinkage of surface water sources, notably sharp decreases caused by extreme climate conditions.[1, 2] Municipal wastewater reuse offers the potential to significantly increase the nation's total available water resources. Approximately 12 billion gallons of municipal wastewater effluent are discharged each day in the U.S., which is equivalent to 27% of the total public water supply.[3] However, only about 10% of the wastewater effluent is actively reused nationwide.[3] One major challenge to recycling is the development of efficient and cost-effective purification processes. Wastewater effluent is widely compromised by sewage produced from growing populations, industries and agriculture. Trace organic chemicals including petroleum hydrocarbons, pharmaceuticals, personal care products, and industrial solvents are often present in the effluent.[4-13]

To minimize the presence of trace organic chemicals, different advanced oxidation processes (AOPs) have been employed.[14-19] The most widely applied approach is based on the photolysis of hydrogen peroxide (H_2O_2) to produce hydroxyl radical ($OH^{\bullet}$). In recent years, sulfate radical ($SO_4^{\bullet-}$) has garnered much attention as an alternative oxidant for AOP.[20-22] In these processes, $SO_4^{\bullet-}$ is typically generated via UV

photolysis of persulfate ($S_2O_8^{2-}$) for water reuse applications.[23-26] $SO_4^{\bullet-}$ has a similar oxidizing power to $OH^{\bullet}$, yet possessing selectively higher reaction rates with electron-rich contaminants that are typically observed in wastewater effluent.[27-30] Due to a higher quantum yield, the rate of $S_2O_8^{2-}$ photolysis is 40% higher than that of H_2O_2 under UV irradiation at 254 nm (a typical wavelength used in UV lamps).[31] Furthermore, the scavenging effect of $S_2O_8^{2-}$ on $SO_4^{\bullet-}$ is two orders of magnitude lower than the scavenging effect of H_2O_2 on $OH^{\bullet}$,[32, 33] which leads to a higher yield of $SO_4^{\bullet-}$ from $S_2O_8^{2-}$ than that of $OH^{\bullet}$ from H_2O_2. These chemical features make $SO_4^{\bullet-}$-based AOP an attractive option for water reuse.

Considering these prospective applications of $SO_4^{\bullet-}$-based oxidation processes for water reuse, it is important to predict the reaction kinetics of $SO_4^{\bullet-}$-driven oxidation reactions with organic contaminants that are present in wastewater effluent. Although some of the radical-driven rate constants can be measured using experimental techniques, *e.g.*, electron pulse radiolysis and γ radiation,[34, 35] it is logistically unrealistic to experimentally measure the rates of every contaminant with short-lived radical species. In addition, the activation energies of $SO_4^{\bullet-}$ with different benzene-derived contaminants are largely unknown, and understanding the activation energies in possible degradation pathways of organic contaminants on a fundamental level are required for predicting byproduct formation in $SO_4^{\bullet-}$ based oxidative water treatment.

Recently, density functional theory (DFT) calculations have started to become commonplace as computational tools for predicting reaction mechanisms and activation energies in redox reactions of environmental significance. There has been recent work

using quantum chemical techniques to estimate reaction barriers and thermodynamic relations in the degradation of trace organic contaminants, especially via the oxidation of $OH^{\bullet}$ or ozone (O_3).[36-41] Due to the complexity of the chemical species examined, these prior studies largely used popular computationally-efficient DFT methods to systematically explore and assess the relativities of contaminants in the aqueous phase. However, most DFT methods are heavily parameterized against a training set of benchmark molecules, *i.e.*, typically organic compounds containing only hydrogen, carbon, nitrogen, and oxygen.[42-44] Specifically, these DFT methods were developed to minimize errors on a given training set of molecules; however, for systems and properties *outside* the training set, Burke and co-workers have demonstrated that these extrapolations can be prone to large and unpredictable deviations.[45] As a result, additional high-level wavefunction based methods are essential to assess whether popular DFT methods are sufficiently accurate for modeling activation energies and thermochemistry, particularly for *inorganic* species outside typical DFT training sets, in environmental computational studies.

The purpose of this study is to assess the accuracy of popular DFT and high-level wavefunction-based methods in quantifying the activation energies of benzene-derived contaminants reacting with $SO_4^{\bullet-}$. Figure 2.1 depicts the chemical structures of the various benzene-derived organic contaminants, and Figure 2.2 shows the two steps of oxidation reaction investigated in this work. Step 1 involves the addition of $SO_4^{\bullet-}$ to form a benzene-derivative cationic radical and the SO_4^{2-} anion. The addition of hydroxide OH^- to the benzene-derivative cation in Step 2 gives the final hydroxylated oxidation product. We examined a wide set of reactions (110 forward and reverse reactions, in total) using a

variety of computational techniques including DFT, MP2/MP4 perturbation theory methods, and high-level coupled cluster CCSD/CCSD(T) approaches. Statistical analyses were carried out for all of these reactions to assess the strengths and limitations of each of the computational methods. We concluded with a discussion and assessment of the specific methods that provide the best accuracy in describing these specific reaction processes relevant to $SO_4^{\bullet-}$ based oxidative water treatments.

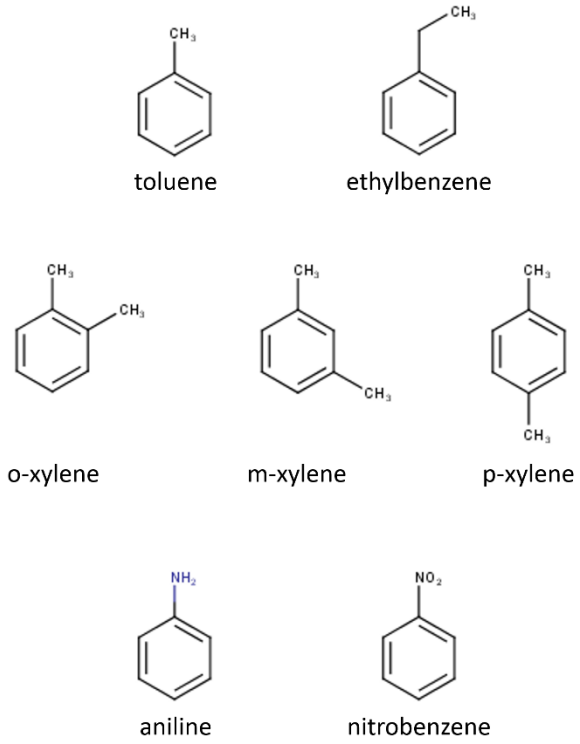

Figure 2.1. Chemical structures of benzene-derived organic contaminants investigated in this work.

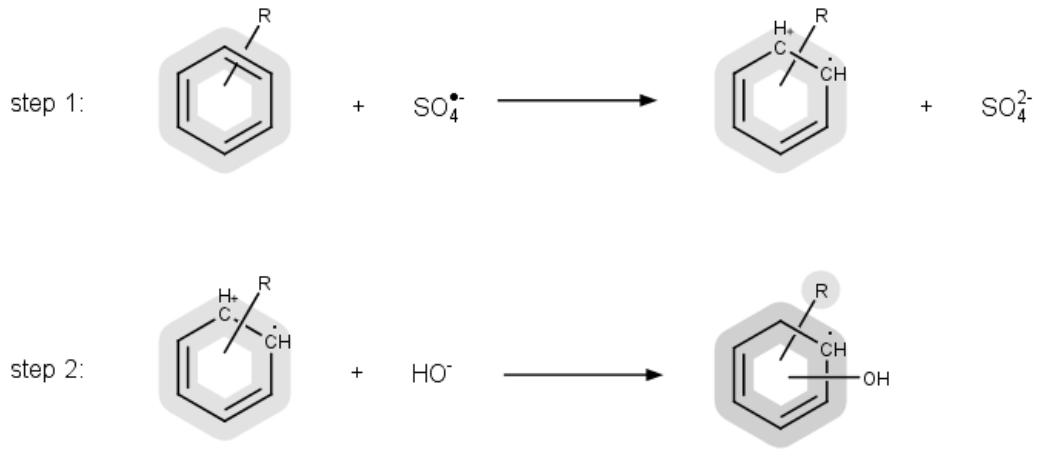

Figure 2.2. Reaction steps investigated in this work: Step 1 involves the addition of $SO_4^{\bullet-}$ to form a benzene-derivative cation and the SO_4^{2-} anion. The *R* group represents the different functional groups depicted previously in Figure 2.1. Step 2 involves the addition of OH^- to the benzene-derivative cation that gives the final hydroxylated product.

II. Computational Methods

For all of the chemical species investigated in this work, we benchmarked the performance of the highly-parametrized M06-2X DFT functional[46] against the wavefunction-based MP2,[47, 48] MP4(SDQ),[49, 50] CCSD,[51, 52] and CCSD(T)[53] methods. The M06-2X exchange-correlation functional[46] includes 54% Hartree-Fock exchange and has been utilized to study a broad spectrum of chemical species and reactions.[54-59] The MP2[47, 48] and MP4(SDQ)[49, 50] wavefunction-based methods incorporate a Møller-Plesset correlation correction[60] to the total energy based on perturbation theory truncated at second order and fourth order for MP2[47, 48] and MP4(SDQ),[49, 50] respectively. The CCSD[61, 62] and CCSD(T)[53] methods utilize a coupled cluster approach including both single and double excitations (and triple excitations for the CCSD(T) method) to obtain highly accurate total energies. The higher-level CCSD and CCSD(T) theoretical approaches typically provide

extremely accurate energies and reaction rates, albeit at a high computational cost. In order to maintain a consistent comparison across the M06-2X, MP2, MP4(SDQ), CCSD, and CCSD(T) levels of theory, the same ground-state and transition-state geometries for all methods were used. Both the ground-state and transition-state geometries were obtained optimized at the M06-2X/6-311+G(d,p) level of theory, and all transition states were confirmed to be first-order saddle points by verifying the presence of a single imaginary harmonic frequency. It is worth mentioning that a complete characterization of a transition state geometry requires a full analysis of the intrinsic reaction coordinate (IRC); however, due to the large number of reactions considered in this study (110 forward/reverse reactions) and the immense computational expense of IRC calculations, we only characterized these transition states with a frequency analysis and reserved the more complete IRC calculations for a future study. For all of the chemical species and computational methods in this study, we utilized the conductor-like polarizable continuum model (PCM) devised by Tomasi and co-workers[63-67] which creates a solute cavity via a set of overlapping spheres to calculate the solvent reaction field.

For all of the wavefunction-based methods (MP2, MP4(SDQ), CCSD, and CCSD(T)) in this study, the same 6-311+G(d,p) basis was also used to calculate total energies for both the ground- and transition-state geometries. Throughout this work we used the CCSD(T) energies as reference values to assess the quality for all of the various methods. We have previously found that the CCSD(T) method accurately reproduces experimental activation energies[68, 69] and electronic properties[70] of various hydrocarbons. As an additional verification on the quality of the CCSD(T) benchmarks, we checked for

possible deficiencies inherent to the single-reference coupled cluster approach. Specifically, for open-shell systems, Schaefer and co-workers[71] proposed an open-shell "T1 diagnostic" to determine whether the single-reference-based CCSD procedure is appropriate or requires a higher-level multi-reference treatment. Based on their criterion, if the Euclidean norm of the t1 vector from an open-shell CCSD calculation is greater than 0.044, a higher-level multireference method is necessary. We have computed the T1 diagnostic for all of the geometry-optimized chemical species in this work and found that none of the systems in this study required a multi-reference treatment of electron correlation (open-shell T1 diagnostic values were in the 0.026 – 0.039 range), indicating that all of the chemical species in this study are accurately described by the coupled-cluster approach. All calculations were carried out with the Gaussian 09 package.[72]

III. Results and Discussion

Before proceeding to a detailed discussion of activation energies for the various reactions, we first carried out a series of two high-level benchmark calculations to assess (1) the robustness of the M06-2X optimized geometries and (2) the accuracy of the 6-311+G(d,p) basis set. Due to the computational complexity of these benchmarks, we only performed these calculations on the 1-aminophenol transition-state and final product, as shown in Figure 2.3 (as a side note, these benchmark calculations were extremely computationally intensive, with the largest of these calculations taking up to *6 continuous days* on 16 × 2.3 GHz AMD Opteron CPUs and *over 230 GB of disk space* on rapid-access solid state drive storage). To assess the robustness of the M06-2X optimized geometries,

we calculated CCSD single-point energies on top of CCSD and M06-2X optimized geometries for the 1-aminophenol transition-state and final product. Figure 2.3(a) shows that the difference in CCSD single-point energies obtained from the CCSD and M06-2X optimized geometries is negligible (less than 0.2 kcal/mol), indicating that the M06-2X geometries used throughout this work are reliable. With the M06-2X optimized geometries verified, we next assessed the accuracy of the 6-311+G(d,p) basis set by comparing CCSD(T)/aug-cc-pvtz and CCSD(T)/6-311+G(d,p) single-point energies on top of the same M06-2X optimized geometries used in Figure 2.3(a). Figure 2.3(b) shows that the difference between the correlation-consistent aug-cc-pvtz and the smaller 6-311+G(d,p) basis set is also relatively small (less than 0.65 kcal/mol), indicating that the 6-311+G(d,p) basis set can be safely used for calculating the thermochemical properties for the numerous reactions (110 forward/reverse reactions) evaluated in this computational study.

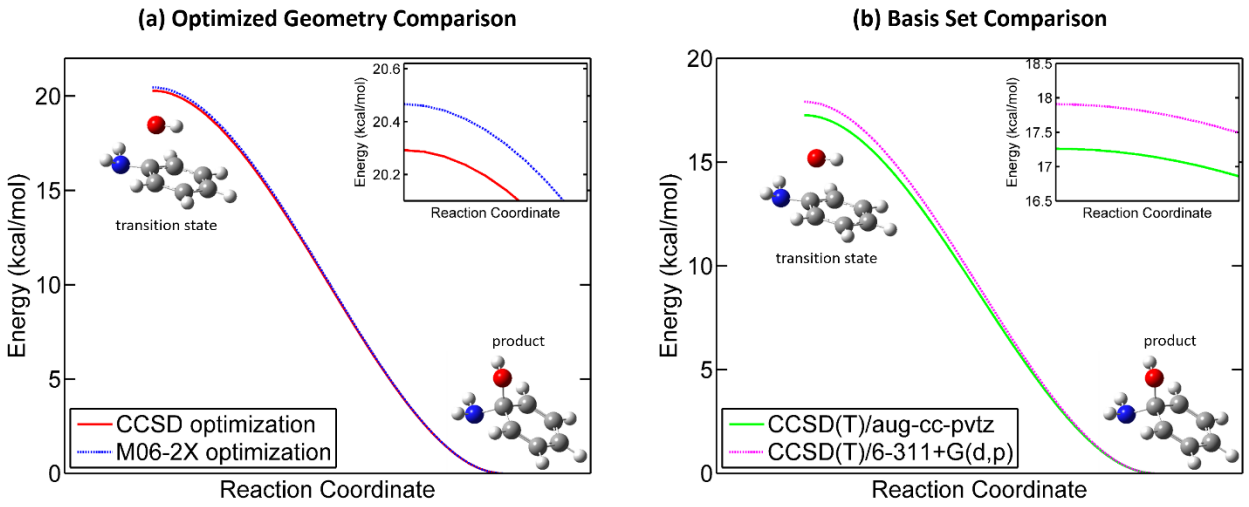

Figure 2.3. Comparison of (a) CCSD single-point energies on top of CCSD and M06-2X optimized geometries and (b) CCSD(T)/aug-cc-pvtz and CCSD(T)/6-311+G(d,p) single-point energies on top of M06-2X optimized geometries for 1-aminophenol. The insets in each of the figures show a magnified portion of the potential energy surface near the transition state, indicating a small energy difference among the various computational methods used in each of the figures.

With these benchmark tests validating our computational approach, we then examined the activation energies for the initial reaction step involving the addition of $SO_4^{\bullet-}$ to the various benzene-derived contaminants. For each of the contaminant, there are multiple sites on the benzene ring that the $SO_4^{\bullet-}$ radical can attach to in the transition state structure. As an example, Figure 2.4 depicts the various transition state structures involved in the following reaction: toluene + $SO_4^{\bullet-}$ → toluene cation + SO_4^{2-}. We explored all of these possible transition-state geometries for toluene as well as for *all* the chemical species (25 transition states in total) depicted in Figure 2.1. Using the CCSD(T) activation energies, E_a, as benchmarks, we performed a mean absolute error (MAE) analysis for both the forward and reverse activation energies involving $SO_4^{\bullet-}$ and the various chemical species, which is summarized in Table 2.1. Figure 2.5 depicts in more detail the general trends in

the forward and reverse activation energies between the various quantum chemical methods. The diagonal line in all of these figures represents an ideal 100% agreement between the CCSD(T) energies and the other computational methods. It is important to mention that the R^2 values listed in Table 2.1 were obtained from a simple linear fit to the data points themselves and not calculated with respect to the diagonal lines shown in Figure 2.5. From the results shown in Figure 2.5, it is worth mentioning that the calculated forward activation energy in step 1 is larger than its reverse activation energy; however, the product of the forward reaction in step 1 (i.e., the benzene cation radical) can further react with OH^- via the forward reaction in step 2 (Figure 2.2). As discussed further in the paragraphs below, the forward activation energy in step 2 is lower than reverse activation energy in step 1. As a result, the rate-limiting step is the forward reaction involving a benzene-derived compound and $SO_4^{\bullet-}$, and once this energy barrier is overcome, the benzene-derivative cation radical will further react with OH^- to generate the hydroxylated product.

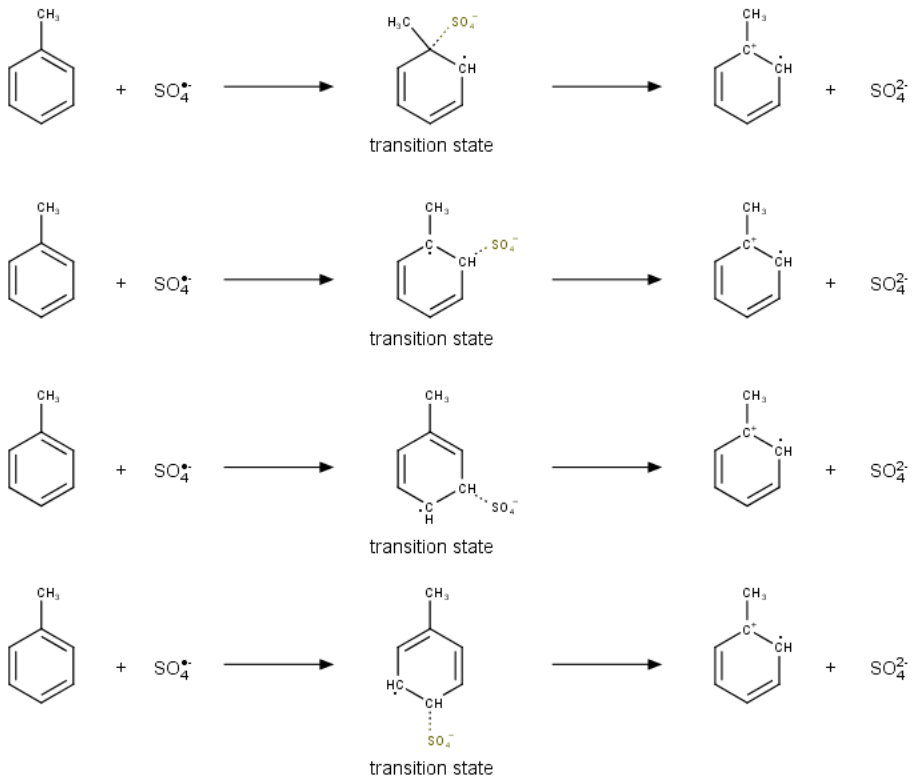

Figure 2.4. Reactants, transition states, and products for the first reaction step involving addition of $SO_4^{\bullet -}$ to toluene.

Table 2.1. Mean absolute error (MAE) with respect to CCSD(T) benchmarks and R^2 fit values for various activation energies (E_a) computed with the M06-2X, MP2, MP4(SDQ), and CCSD methods

	M06-2X		MP2		MP4(SDQ)		CCSD	
	MAE (kcal/mol)	R^2	MAE (kcal/mol)	R^2	MAE (kcal/mol)	R^2	MAE (kcal/mol)	R^2
Forward E_a for $SO_4^{\bullet-}$ addition	3.35	0.95	19.34	0.69	8.23	0.83	1.02	0.99
Reverse E_a for $SO_4^{\bullet-}$ addition	2.00	0.99	15.37	0.38	10.11	0.86	4.20	1.00
Forward E_a for OH^- addition	0.88	0.99	17.51	0.83	9.56	0.96	1.69	1.00
Reverse E_a for OH^- addition	0.49	0.88	8.26	0.81	6.34	0.91	2.27	0.99

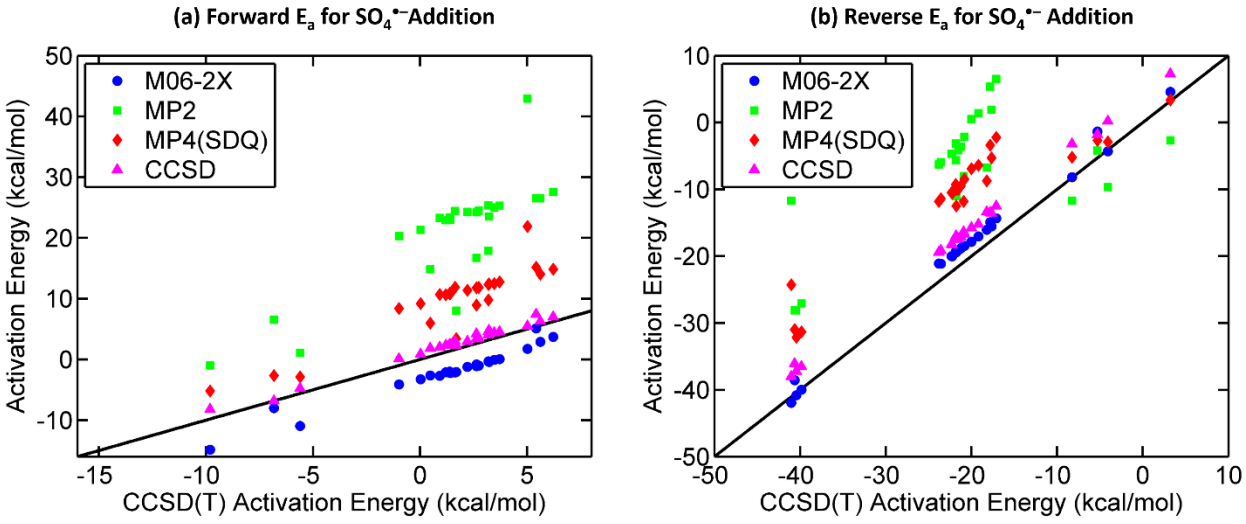

Figure 2.5. Predicted activation energies of the (a) forward and (b) reverse reactions of various benzene derivatives reacting with $SO_4^{\bullet-}$. The diagonal line in each figure represents a perfect match to the benchmark CCSD(T) activation energies.

Both Table 2.1 and Figure 2.5 show that the CCSD calculations (MAE = 1.02 kcal/mol) are in excellent agreement with the CCSD(T) benchmarks for the forward activation energy for the $SO_4^{\bullet-}$ addition. The M06-2X calculations have errors that are quite higher (MAE = 3.35 kcal/mol), followed by the MP4(SDQ) and MP2 methods which have even larger MAEs of 8.23 and 19.34 kcal/mol, respectively. Upon examining the reverse activation energy for the $SO_4^{\bullet-}$ addition, we surprisingly find that the M06-2X functional significantly outperforms the CCSD method by a factor of 2 with respect to the total MAE. Again, the MP4(SDQ) and MP2 methods incur larger errors compared to either the CCSD or M06-2X calculations for the reverse activation energy for the $SO_4^{\bullet-}$ addition. We also note that the CCSD and M06-2X calculations exhibit a high degree of statistical correlation (R^2 = 0.95 – 1.00) for both the forward and reverse activation energy for the $SO_4^{\bullet-}$ addition, indicating that the errors in each of these computational methods is systematic rather than random.

We next examined the activation energies for the second reaction step involving the addition of OH^- to the various benzene-derived cation radicals. As before, for each of the benzene cation radical, there are multiple sites on the benzene ring that the OH^- molecule can attach to. As a particular example, Figure 2.6 depicts the various products involved in the addition of OH^- to the toluene cation. Again, we explored all of these possible transition-state geometries for toluene as well as for *all* the chemical species (30 transition states in total) depicted in Figure 2.1, yielding the various products shown in Figure 2.6. A mean absolute error (MAE) analysis was carried out for both the forward and reverse activation energies for all of these resulting products using the CCSD(T) activation

energies as benchmarks. Table 2.1 and Figure 2.7 summarize and depict the general trends in the forward and reverse activation energies between the various quantum chemical methods.

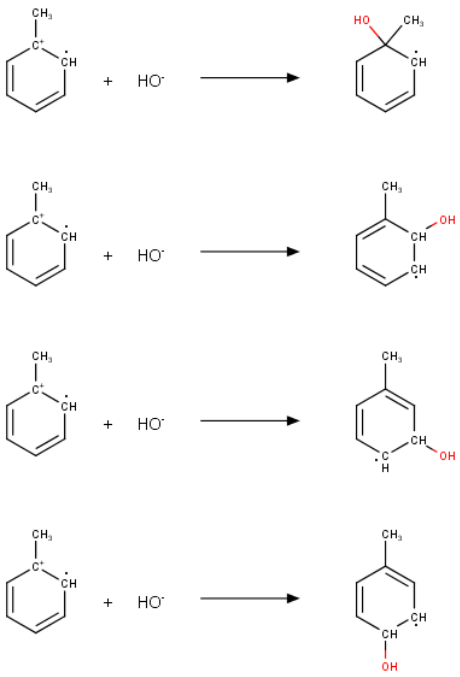

Figure 2.6. Reactants and products for the second reaction step involving addition of OH^- to toluene.

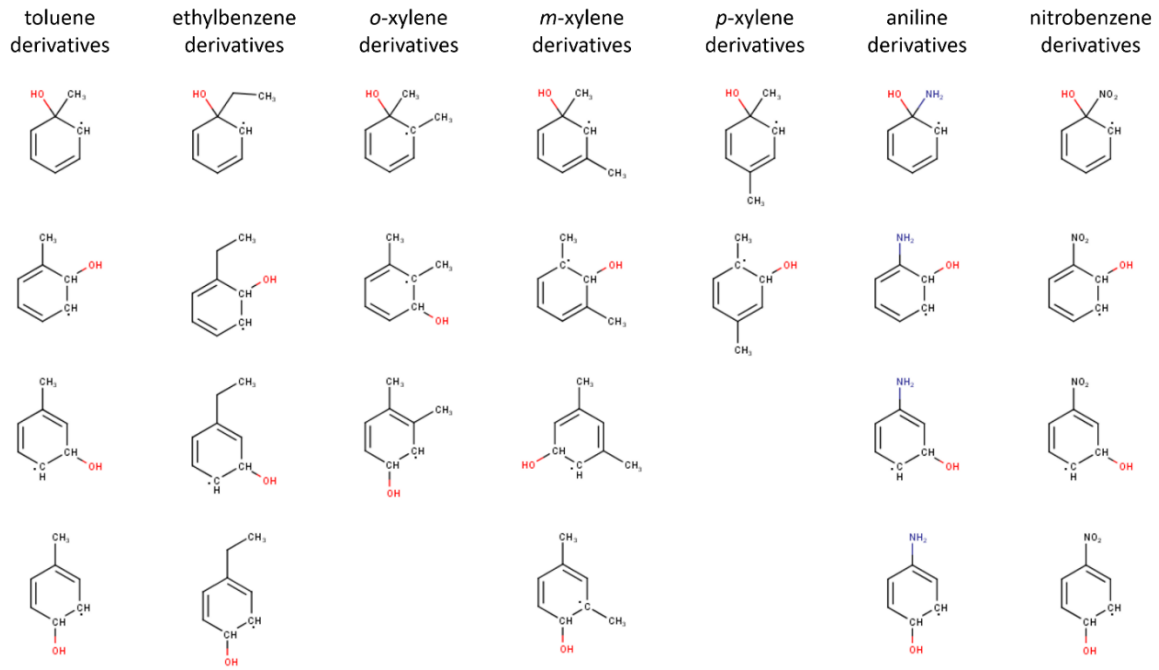

Figure 2.7. All possible products resulting from the reaction of various hydroxylated oxidation products from oxidation of benzene derivatives by sulfate radical and subsequent OH^- addition. The energies of the various products were computed using both DFT and high-level wavefunction based methods to assess the accuracy of all the computational methods used in the main text.

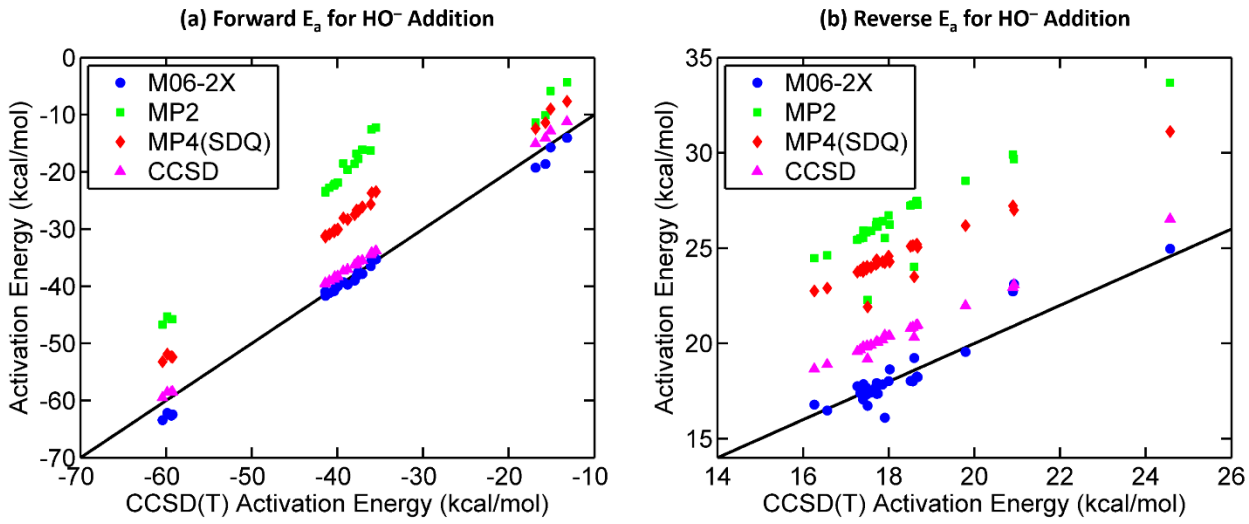

Figure 2.8. Predicted activation energies of the (a) forward and (b) reverse reactions of benzene-derived cation radical reacting with OH^-. The diagonal line in each figure represents a perfect match to the benchmark CCSD(T) activation energies.

In contrast to the statistical trends for the $SO_4^{\bullet-}$ reaction described previously, we find that the various computational methods more accurately predict the activation energies for the OH^- addition, resulting in lower MAEs in general. In particular, both Table 2.1 and Figure 2.8 actually show that the M06-2X functional outperforms all other methods (even the CCSD method) for both the forward and reverse activation energy for the OH^- addition. However, we note that the M06-2X R^2 values (= 0.88) for the reverse reaction are noticeably worse than the corresponding MP4(SDQ) and CCSD wavefunction-based methods. Consequently, these deviations from $R^2 = 1$ indicate a non-systematic error in the M06-2X activation energies for the reverse reaction for the OH^- addition. As before, the MP4(SDQ) and MP2 methods incur larger errors compared to either the CCSD or M06-2X calculations for both the forward and reverse activation energy for the OH^- addition. These errors are due to the perturbative nature of the MP4(SDQ) and MP2 methods which

do not capture dynamical correlations effects compared to the accurate CCSD(T) calculations. Based on our benchmarks on activation energies alone, we find that the popular M06-2X DFT functional is significantly more accurate for OH^- reactions than for $SO_4^{\bullet-}$ reactions (although further work is needed on assessing the complete reaction pathways). This stark difference in accuracy is due to the training set used to parameterize the M06-2X functional, which primarily consists of hydrocarbon molecules that do not include other non-carbon based environmental species such as $SO_4^{\bullet-}$. As a result, while the M06-2X functional yields impressive (nearly CCSD(T)-quality) accuracy for conventional reactions, we recommend the use of high-level quantum calculations to spot-check environmental chemistry reactions that may lie outside the training set of the M06-2X functional, particularly for water oxidation reactions that involve $SO_4^{\bullet-}$.

IV. Conclusions

In conclusion, we have examined a wide set of reactions (110 forward and reverse reactions, in total) that play an important role in sulfate radical-based oxidation processes for water reuse and groundwater remediation. To understand these complex reactions at a fundamental level, we utilized a variety of computational techniques including DFT, MP2/MP4 perturbation theory methods, and high-level coupled cluster CCSD/CCSD(T) approaches. While DFT calculations have started to become commonplace in predicting reaction mechanisms and activation energies in environmental processes, many DFT functionals are highly-parameterized and can fail dramatically for chemical species outside of their training set. As a result, additional high-level methods are essential for spot-

checking these results and for iterative feedback between theory and experiment, particularly for accurate calculations of reaction mechanisms in environmental chemistry. Within this comprehensive study, which involves over 100 reactions and 5 different computational methods, we found that the popular M06-2X functional is more accurate for OH^- reactions than for $SO_4^{\bullet-}$ reactions (based on high-level CCSD(T) calculations used as benchmarks). In general, we find that the M06-2X functional does perform reasonably well for both OH^- and $SO_4^{\bullet-}$ reactions; however, we noticed a low degree of statistical correlation for the reverse activation energy barriers in the OH^- reactions. As a result, while the M06-2X functional yields impressive (nearly CCSD(T)-quality) accuracy for conventional reactions, high-level benchmarks should be carried out to spot-check reactions that may lie outside the training set of M06-2X (such as reactions that involve $SO_4^{\bullet-}$ or other inorganic oxidants). These extensive calculations and methodological assessments provide a predictive path towards understanding increasingly more complex reaction mechanisms in environmental processes.

V. References

1. Bufe, M., What took us so long? Direct potable-water reuse debuts in Texas. *Water Environment & Technology* August, 2013.

2. Trenberth, K. E., Changes in precipitation with climate change. *Climate Research* **2011,** *47*, 123-138.

3. National Research Council (U.S.). Committee on the Assessment of Water Reuse as an Approach for Meeting Future Water Supply Needs.; National Research Council (U.S.). Committee on the Assessment of Water Reuse as an Approach for Meeting Future Water Supply Needs., Water reuse potential for expanding the nation's water supply through reuse of municipal wastewater. National Academies Press,: Washington, D.C., 2012; pp 1 online resource (xiii, 262 p.).

4. Snyder, S. A. *Evaluation of Conventional and Advanced Treatment Processes to Remove Endocrine Disruptors and Pharmaceutically Active Compounds. American Water Works Research Foundation Report.*: Denver, CO, 2007.

5. Steffen, M. M.; Zhu, Z.; McKay, R. M. L.; Wilhelm, S. W.; Bullerjahn, G. S., Taxonomic assessment of a toxic cyanobacteria shift in hypereutrophic Grand Lake St. Marys (Ohio, USA). *Harmful Algae* **2014,** *33*, 12-18.

6. Stackelberg, P. E.; Furlong, E. T.; Meyer, M. T.; Zaugg, S. D.; Henderson, A. K.; Reissman, D. B., Persistence of pharmaceutical compounds and other organic wastewater contaminants in a conventional drinking-watertreatment plant. *Science of the Total Environment* **2004,** *329*, 99-113.

7. Mompelat, S.; Le Bot, B.; Thomas, O., Occurrence and fate of pharmaceutical products and by-products, from resource to drinking water. *Environment International* **2009,** *35*, 803-814.

8. Westerhoff, P.; Yoon, Y.; Snyder, S.; Wert, E., Fate of endocrine-disruptor, pharmaceutical, and personal care product chemicals during simulated drinking water treatment processes. *Environmental Science & Technology* **2005,** *39*, 6649-6663.

9. Kleywegt, S.; Pileggi, V.; Yang, P.; Hao, C. Y.; Zhao, X. M.; Rocks, C.; Thach, S.; Cheung, P.; Whitehead, B., Pharmaceuticals, hormones and bisphenol A in untreated source and finished drinking water in Ontario, Canada - and treatment efficiency. *Science of the Total Environment* **2011,** *409*, 1481-1488.

10. Mompelat, S.; Thomas, O.; Le Bot, B., Contamination levels of human pharmaceutical compounds in French surface and drinking water. *Journal of Environmental Monitoring* **2011,** *13*, 2929-2939.

11. Valcarcel, Y.; Alonso, S. G.; Rodriguez-Gil, J. L.; Gil, A.; Catala, M., Detection of pharmaceutically active compounds in the rivers and tap water of the Madrid Region (Spain) and potential ecotoxicological risk. *Chemosphere* **2011,** *84*, 1336-1348.

12. Benotti, M. J.; Trenholm, R. A.; Vanderford, B. J.; Holady, J. C.; Stanford, B. D.; Snyder, S. A., Pharmaceuticals and Endocrine Disrupting Compounds in US Drinking Water. *Environmental Science & Technology* **2009,** *43*, 597-603.

13. Huerta-Fontela, M.; Galceran, M. T.; Ventura, F., Occurrence and removal of pharmaceuticals and hormones through drinking water treatment. *Water Research* **2011,** *45*, 1432-1442.

14. Raut-Jadhav, S.; Saharan, V. K.; Pinjari, D.; Sonawane, S.; Saini, D.; Pandit, A., Synergetic effect of combination of AOP's (hydrodynamic cavitation and H2O2) on the degradation of neonicotinoid class of insecticide. *Journal of Hazardous Materials* **2013,** *261*, 139-147.

15. Saharan, V. K.; Badve, M. P.; Pandit, A. B., Degradation of Reactive Red 120 dye using hydrodynamic cavitation. *Chemical Engineering Journal* **2011,** *178*, 100-107.

16. Lee, C.; Sedlak, D. L., A novel homogeneous Fenton-like system with Fe(III)-phosphotungstate for oxidation of organic compounds at neutral pH values. *Journal of Molecular Catalysis a-Chemical* **2009,** *311*, 1-6.

17. An, J. J.; Zhu, L. H.; Zhang, Y. Y.; Tang, H. Q., Efficient visible light photo-Fenton-like degradation of organic pollutants using in situ surface-modified BiFeO3 as a catalyst. *Journal of Environmental Sciences* **2013,** *25*, 1213-1225.

18. Bahnmuller, S.; Loi, C. H.; Linge, K. L.; von Gunten, U.; Canonica, S., Degradation rates of benzotriazoles and benzothiazoles under UV-C irradiation and the advanced oxidation process UV/H2O2. *Water Research* **2015,** *74*, 143-154.

19. Moreira, F. C.; Boaventura, R. A. R.; Brillas, E.; Vilar, V. J. P., Remediation of a winery wastewater combining aerobic biological oxidation and electrochemical advanced oxidation processes. *Water Research* **2015,** *75*, 95-108.

20. He, X. X.; de la Cruz, A. A.; O'Shea, K. E.; Dionysiou, D. D., Kinetics and mechanisms of cylindrospermopsin destruction by sulfate radical-based advanced oxidation processes. *Water Research* **2014,** *63*, 168-178.

21. Antoniou, M. G.; de la Cruz, A. A.; Dionysiou, D. D., Intermediates and Reaction Pathways from the Degradation of Microcystin-LR with Sulfate Radicals. *Environmental Science & Technology* **2010,** *44*, 7238-7244.

22. Liu, H. Z.; Bruton, T. A.; Li, W.; Van Buren, J.; Prasse, C.; Doyle, F. M.; Sedlak, D. L., Oxidation of Benzene by Persulfate in the Presence of Fe(III)- and Mn(IV)-Containing Oxides: Stoichiometric Efficiency and Transformation Products. *Environmental Science & Technology* **2016,** *50*, 890-898.

23. Lutze, H. V.; Bakkour, R.; Kerlin, N.; von Sonntag, C.; Schmidt, T. C., Formation of bromate in sulfate radical based oxidation: Mechanistic aspects and suppression by dissolved organic matter. *Water Research* **2014,** *53*, 370-377.

24. Qian, Y. J.; Guo, X.; Zhang, Y. L.; Peng, Y.; Sun, P. Z.; Huang, C. H.; Niu, J. F.; Zhou, X. F.; Crittenden, J. C., Perfluorooctanoic Acid Degradation Using UV-Persulfate Process: Modeling of the Degradation and Chlorate Formation. *Environmental Science & Technology* **2016,** *50*, 772-781.

25. Zhang, R. C.; Sun, P. Z.; Boyer, T. H.; Zhao, L.; Huang, C. H., Degradation of Pharmaceuticals and Metabolite in Synthetic Human Urine by UV, UV/H2O2, and UV/PDS. *Environmental Science & Technology* **2015,** *49*, 3056-3066.

26. Yang, Y.; Pignatello, J. J.; Ma, J.; Mitch, W. A., Comparison of Halide Impacts on the Efficiency of Contaminant Degradation by Sulfate and Hydroxyl Radical-Based Advanced Oxidation Processes (AOPs). *Environmental Science & Technology* **2014,** *48*, 2344-2351.

27. Minisci, F.; Citterio, A.; Giordano, C., ELECTRON-TRANSFER PROCESSES - PEROXYDISULFATE, A USEFUL AND VERSATILE REAGENT IN ORGANIC-CHEMISTRY. *Accounts of Chemical Research* **1983,** *16*, 27-32.

28. Neta, P.; Madhavan, V.; Zemel, H.; Fessenden, R. W., RATE CONSTANTS AND MECHANISM OF REACTION OF SO4.- WITH AROMATIC-COMPOUNDS. *Journal of the American Chemical Society* **1977,** *99*, 163-164.

29. Peyton, G. R., THE FREE-RADICAL CHEMISTRY OF PERSULFATE-BASED TOTAL ORGANIC-CARBON ANALYZERS. *Marine Chemistry* **1993,** *41*, 91-103.

30. Liu, H. Z.; Bruton, T. A.; Doyle, F. M.; Sedlak, D. L., In Situ Chemical Oxidation of Contaminated Groundwater by Persulfate: Decomposition by Fe(III)- and Mn(IV)-Containing Oxides and Aquifer Materials. *Environmental Science & Technology* **2014,** *48*, 10330-10336.

31. Li, W.; Jain, T.; Ishida, K.; Liu, H., A mechanistic understanding of the degradation of trace organic contaminants by UV/hydrogen peroxide, UV/persulfate and UV/free chlorine for water reuse. *Environmental Science: Water Research & Technology* **2017**.

32. Das, T. N., Reactivity and role of SO5 center dot- radical in aqueous medium chain oxidation of sulfite to sulfate and atmospheric sulfuric acid generation. *Journal of Physical Chemistry A* **2001,** *105*, 9142-9155.

33. Buxton, G. V.; Greenstock, C. L.; Helman, W. P.; Ross, A. B., CRITICAL-REVIEW OF RATE CONSTANTS FOR REACTIONS OF HYDRATED ELECTRONS, HYDROGEN-ATOMS AND HYDROXYL RADICALS (.OH/.O-) IN AQUEOUS-SOLUTION. *Journal of Physical and Chemical Reference Data* **1988,** *17*, 513-886.

34. Ben Abdelmelek, S.; Greaves, J.; Ishida, K. P.; Cooper, W. J.; Song, W. H., Removal of Pharmaceutical and Personal Care Products from Reverse Osmosis Retentate Using Advanced Oxidation Processes. *Environmental Science & Technology* **2011,** *45*, 3665-3671.

35. Patton, S.; Li, W.; Couch, K. D.; Mezyk, S. P.; Ishida, K. P.; Liu, H., Impact of the Ultraviolet Photolysis of Monochloramine on 1,4-Dioxane Removal: New Insights into Potable Water Reuse. *Environmental Science & Technology Letters* **2017,** *4*, 26-30.

36. Minakata, D.; Li, K.; Westerhoff, P.; Crittenden, J., Development of a Group Contribution Method To Predict Aqueous Phase Hydroxyl Radical (HO center dot) Reaction Rate Constants. *Environmental Science & Technology* **2009,** *43*, 6220-6227.

37. Naumov, S.; von Sonntag, C., Standard Gibbs Free Energies of Reactions of Ozone with Free Radicals in Aqueous Solution: Quantum-Chemical Calculations. *Environmental Science & Technology* **2011,** *45*, 9195-9204.

38. Minakata, D.; Crittenden, J., Linear Free Energy Relationships between Aqueous phase Hydroxyl Radical Reaction Rate Constants and Free Energy of Activation. *Environmental Science & Technology* **2011,** *45*, 3479-3486.

39. Arnold, W. A.; Oueis, Y.; O'Connor, M.; Rinaman, J. E.; Taggart, M. G.; McCarthy, R. E.; Foster, K. A.; Latch, D. E., QSARs for phenols and phenolates: oxidation potential as a predictor of reaction rate constants with photochemically produced oxidants. *Environmental Science: Processes & Impacts* **2017**.

40. Trogolo, D.; Mishra, B. K.; Heeb, M. B.; von Gunten, U.; Arey, J. S., Molecular Mechanism of NDMA Formation from N,N-Dimethylsulfamide During Ozonation:

Quantum Chemical Insights into a Bromide-Catalyzed Pathway. *Environmental Science & Technology* **2015,** *49*, 4163-4175.

41. Lee, M.; Blum, L.; Schmid, E.; Fenner, K.; von Gunten, U., A computer-based prediction platform for the reaction of ozone with organic compounds in aqueous solution: Kinetics and mechanisms. *Environmental Science: Processes & Impacts* **2017**.

42. Becke, A. D., Density-Functional Thermochemistry .3. The Role of Exact Exchange. *J Chem Phys* **1993,** *98*, 5648-5652.

43. Becke, A. D., A New Mixing of Hartree-Fock and Local Density-Functional Theories. *J Chem Phys* **1993,** *98*, 1372-1377.

44. Medvedev, M. G.; Bushmarinov, I. S.; Sun, J.; Perdew, J. P.; Lyssenko, K. A., Density functional theory is straying from the path toward the exact functional. *Science* **2017,** *355*, 49-52.

45. Rappoport, D.; Crawford, N. R. M.; Furche, F.; Burke, K., Approximate Density Functionals: Which Should I Choose? In *Encyclopedia of Inorganic Chemistry*, John Wiley & Sons, Ltd2006.

46. Zhao, Y.; Truhlar, D. G., The M06 suite of density functionals for main group thermochemistry, thermochemical kinetics, noncovalent interactions, excited states, and transition elements: two new functionals and systematic testing of four M06-class functionals and 12 other functionals. *Theor Chem Acc* **2008,** *120*, 215-241.

47. Head-Gordon, M.; Pople, J. A.; Frisch, M. J., MP2 energy evaluation by direct methods. *Chem Phys Lett* **1988,** *153*, 503-506.

48. Frisch, M. J.; Head-Gordon, M.; Pople, J. A., A direct MP2 gradient method. *Chem Phys Lett* **1990,** *166*, 275-280.

49. Trucks, G. W.; Watts, J. D.; Salter, E. A.; Bartlett, R. J., Analytical MBPT(4) gradients. *Chem Phys Lett* **1988,** *153*, 490-495.

50. Trucks, G. W.; Salter, E. A.; Sosa, C.; Bartlett, R. J., Theory and implementation of the MBPT density matrix. An application to one-electron properties. *Chem Phys Lett* **1988,** *147*, 359-366.

51. Purvis, G. D.; Bartlett, R. J., A FULL COUPLED-CLUSTER SINGLES AND DOUBLES MODEL - THE INCLUSION OF DISCONNECTED TRIPLES. *Journal of Chemical Physics* **1982,** *76*, 1910-1918.

52. Scuseria, G. E.; Janssen, C. L.; Schaefer, H. F., AN EFFICIENT REFORMULATION OF THE CLOSED-SHELL COUPLED CLUSTER SINGLE AND DOUBLE EXCITATION (CCSD) EQUATIONS. *Journal of Chemical Physics* **1988,** *89*, 7382-7387.

53. Pople, J. A.; Head-Gordon, M.; Raghavachari, K., Quadratic configuration interaction. A general technique for determining electron correlation energies. *The Journal of Chemical Physics* **1987,** *87*, 5968-5975.

54. Zhao, Y.; Truhlar, D. G., How Well Can New-Generation Density Functionals Describe the Energetics of Bond-Dissociation Reactions Producing Radicals? *The Journal of Physical Chemistry A* **2008,** *112*, 1095-1099.

55. Hohenstein, E. G.; Chill, S. T.; Sherrill, C. D., Assessment of the Performance of the M05−2X and M06−2X Exchange-Correlation Functionals for Noncovalent Interactions in Biomolecules. *J Chem Theory Comput* **2008,** *4*, 1996-2000.

56. Isiklan, M.; Saeed, M. A.; Pramanik, A.; Wong, B. M.; Fronczek, F. R.; Hossain, M. A., A C-3 Symmetric Nitrate Complex with a Thiophene-Based Tripodal Receptor. *Crystal Growth & Design* **2011,** *11*, 959-963.

57. Hossain, M. A.; Saeed, M. A.; Fronczek, F. R.; Wong, B. M.; Dey, K. R.; Mendy, J. S.; Gibson, D., Charge-Assisted Encapsulation of Two Chlorides by a Hexaprotonated Azamacrocycle. *Crystal Growth & Design* **2010,** *10*, 1478-1481.

58. Saeed, M. A.; Wong, B. M.; Fronczek, F. R.; Venkatraman, R.; Hossain, M. A., Formation of an Amine-Water Cyclic Pentamer: A New Type of Water Cluster in a Polyazacryptand. *Crystal Growth & Design* **2010,** *10*, 1486-1488.

59. Saeed, M. A.; Pramanik, A.; Wong, B. M.; Haque, S. A.; Powell, D. R.; Chand, D. K.; Hossain, M. A., Self-assembly of ordered water tetramers in an encapsulated $[Br(H_2O)_{12}]^-$ complex. *Chem Commun* **2012,** *48*, 8631-8633.

60. Møller, C.; Plesset, M. S., Note on an Approximation Treatment for Many-Electron Systems. *Physical Review* **1934,** *46*, 618-622.

61. III, G. D. P.; Bartlett, R. J., A full coupled-cluster singles and doubles model: The inclusion of disconnected triples. *The Journal of Chemical Physics* **1982,** *76*, 1910-1918.

62. Scuseria, G. E.; Janssen, C. L.; III, H. F. S., An efficient reformulation of the closed-shell coupled cluster single and double excitation (CCSD) equations. *The Journal of Chemical Physics* **1988,** *89*, 7382-7387.

63. Fortunelli, A.; Tomasi, J., THE IMPLEMENTATION OF DENSITY-FUNCTIONAL THEORY WITHIN THE POLARIZABLE CONTINUUM MODEL FOR SOLVATION. *Chemical Physics Letters* **1994,** *231*, 34-39.

64. Tomasi, J.; Bonaccorsi, R.; Cammi, R.; Delvalle, F. J. O., THEORETICAL CHEMISTRY IN SOLUTION - SOME RESULTS AND PERSPECTIVES OF THE CONTINUUM METHODS AND IN PARTICULAR OF THE POLARIZABLE CONTINUUM MODEL. *Theochem-Journal of Molecular Structure* **1991,** *80*, 401-424.

65. Delvalle, F. J. O.; Bonaccorsi, R.; Cammi, R.; Tomasi, J., ELECTRON CORRELATION AND SOLVATION EFFECTS .3. INFLUENCE OF THE BASIS SET AND THE CHEMICAL-COMPOSITION ON THE SOLVATION ENERGY COMPONENTS EVALUATED WITH THE QUANTUM-MECHANICAL POLARIZABLE CONTINUUM MODEL. *Theochem-Journal of Molecular Structure* **1991,** *76*, 295-312.

66. Delvalle, F. J. O.; Tomasi, J., ELECTRON CORRELATION AND SOLVATION EFFECTS .1. BASIC FORMULATION AND PRELIMINARY ATTEMPT TO INCLUDE THE ELECTRON CORRELATION IN THE QUANTUM-MECHANICAL POLARIZABLE CONTINUUM MODEL SO AS TO STUDY SOLVATION PHENOMENA. *Chemical Physics* **1991,** *150*, 139-150.

67. Aguilar, M. A.; Delvalle, F. J. O.; Tomasi, J., ELECTRON CORRELATION AND SOLVATION EFFECTS .2. THE DESCRIPTION OF THE VIBRATIONAL PROPERTIES OF A WATER MOLECULE IN A DIELECTRIC GIVEN BY THE APPLICATION OF THE POLARIZABLE CONTINUUM MODEL WITH INCLUSION OF CORRELATION-EFFECTS. *Chemical Physics* **1991,** *150*, 151-161.

68. Wong, B. M.; Raman, S., Thermodynamic calculations for molecules with asymmetric internal rotors - Application to 1,3-butadiene. *J Comput Chem* **2007,** *28*, 759-766.

69. Wong, B. M.; Steeves, A. H.; Field, R. W., Electronic signatures of large amplitude motions: Dipole moments of vibrationally excited local-bend and local-stretch states of S-0 acetylene. *J Phys Chem B* **2006,** *110*, 18912-18920.

70. Oviedo, M. B.; Ilawe, N. V.; Wong, B. M., Polarizabilities of π-Conjugated Chains Revisited: Improved Results from Broken-Symmetry Range-Separated DFT and New CCSD(T) Benchmarks. *J Chem Theory Comput* **2016,** *12*, 3593-3602.

71. Rienstra-Kiracofe, J. C.; Tschumper, G. S.; Schaefer, H. F.; Nandi, S.; Ellison, G. B., Atomic and Molecular Electron Affinities: Photoelectron Experiments and Theoretical Computations. *Chem Rev* **2002,** *102*, 231-282.

72. Frisch, M. J.; Trucks, G. W.; Schlegel, H. B.; Scuseria, G. E.; Robb, M. A.; Cheeseman, J. R.; Scalmani, G.; Barone, V.; Mennucci, B.; Petersson, G. A.; Nakatsuji, H.; Caricato, M.; Li, X.; Hratchian, H. P.; Izmaylov, A. F.; Bloino, J.; Zheng, G.; Sonnenberg, J. L.; Hada, M.; Ehara, M.; Toyota, K.; Fukuda, R.; Hasegawa, J.; Ishida, M.; Nakajima, T.; Honda, Y.; Kitao, O.; Nakai, H.; Vreven, T.; Montgomery Jr., J. A.; Peralta, J. E.; Ogliaro, F.; Bearpark, M. J.; Heyd, J.; Brothers, E. N.; Kudin, K. N.; Staroverov, V. N.; Kobayashi, R.; Normand, J.; Raghavachari, K.; Rendell, A. P.; Burant, J. C.; Iyengar, S. S.; Tomasi, J.; Cossi, M.; Rega, N.; Millam, N. J.; Klene, M.; Knox, J. E.; Cross, J. B.; Bakken, V.; Adamo, C.; Jaramillo, J.; Gomperts, R.; Stratmann, R. E.; Yazyev, O.; Austin, A. J.; Cammi, R.; Pomelli, C.; Ochterski, J. W.; Martin, R. L.; Morokuma, K.; Zakrzewski, V. G.; Voth, G. A.; Salvador, P.; Dannenberg, J. J.; Dapprich, S.; Daniels, A. D.; Farkas, Ö.; Foresman, J. B.; Ortiz, J. V.; Cioslowski, J.; Fox, D. J. *Gaussian 09*, Gaussian, Inc.: Wallingford, CT, USA, 2009.

Conclusion

In this thesis, I have presented two examples of predictive simulations that were utilized in the broad areas of nanoscience and environmental chemistry. While these projects have very different scopes, they emphasize the versatility and predictive power of computational materials and quantum chemistry. Specifically, these studies provide predictive trends on electronic properties in graphdiyne nanotubes as well as a comprehensive benchmarks of various computational methods for reaction mechanisms in sulfate oxidation reactions.

For my first project, we provided quantitative predictions on the structural relaxation energy, binding energy per atom, electron/hole mass, and bandgap for armchair and zigzag graphdiyne nanotubes as a function of radius. We established that relaxation energy and bandgap decrease as a function of diameter for both armchair and zigzag graphdiyne nanotubes and provided closed-form simple equations that could be used by experimentalists to estimate the bandgap as a function of diameter. In addition to our quantitative results, we also determined that the zigzag chirality (as opposed to the armchair chirality) caters to greater electron and hole transport due to the delocalization of the HOCO and LUCO along the axis of the wire.

In my second project, we established the feasibility of various computational methods to accurately determine reaction energies of benzene-derived contaminants with sulfate ion and hydroxide. We tested M06-2X DFT calculations, MP2/MP4 perturbation theory methods, and high-level coupled cluster CCSD and CCSD(T) methods. Our findings for these particular reactions show that the M06-2X functional performs

reasonably well, and the various reaction energies are close to the highly accurate CCSD(T) values. Additionally, the M06-2X functional is more accurate for hydroxide reactions than for sulfate ion reactions; however, this particular functional exhibits a low degree of statistical correlation for the reverse activation energy barriers for the hydroxide reactions. While our results indicate that M06-2X is a computationally-efficient approximation for the high level CCSD(T) method, we still advise the use of CCSD(T) for spot-checking the results from DFT calculations. On a side note, our results and work were specially featured as the cover issue of *Environmental Science: Processes & Impacts*.

Predictive simulations provide an essential counterpart for experiments in materials science, chemical, and environmental engineering. In particular, this thesis highlights the use of predictive calculations for graphdiyne nanotubes and provides mechanistic electronic properties of these systems that can be further used in nanoscale science applications and light-harvesting materials. In addition, our study of various computational methods provides a critical assessment of popular DFT methods for predicting reaction mechanisms in environmental chemistry. Taken together, these two studies emphasize the predictive power and efficiency of quantum-mechanical simulations to advance our understanding of material science and chemical engineering processes.

Appendix

Table 1.3. Vibrational frequencies, symmetries, and infrared/Raman analysis for the (2,2) GDNT. IRREP labels refer to the symmetry representation; A and I indicate whether the mode is active or inactive, respectively, for IR and Raman.

MODES	FREQUENCIES (CM**-1)	FREQUENCIES (THZ)	IRREP	IR	RAMAN
1- 2	0.0000	0.0000	(Eu)	A	I
3- 3	0.0000	0.0000	(A2u)	A	I
4- 4	0.0000	0.0000	(A2g)	I	I
5- 6	40.8500	1.2247	(Eg)	I	A
7- 7	57.8766	1.7351	(B2g)	I	A
8- 8	75.9913	2.2782	(B1u)	I	I
9- 9	76.8105	2.3027	(B1g)	I	A
10- 10	78.4954	2.3532	(B2u)	I	I
11- 12	79.5506	2.3849	(Eu)	A	I
13- 13	90.9144	2.7255	(A2u)	A	I
14- 14	99.2787	2.9763	(A2g)	I	I
15- 15	103.5401	3.1041	(B2g)	I	A
16- 17	108.1431	3.2420	(Eg)	I	A
18- 18	116.2301	3.4845	(A1u)	I	I
19- 19	130.4855	3.9119	(A1g)	I	A
20- 21	132.9062	3.9844	(Eg)	I	A
22- 23	141.4979	4.2420	(Eu)	A	I
24- 24	164.0076	4.9168	(A1g)	I	A
25- 25	164.5027	4.9317	(A1u)	I	I
26- 26	165.9325	4.9745	(B2u)	I	I
27- 27	166.9600	5.0053	(A2g)	I	I
28- 28	172.5862	5.1740	(B1g)	I	A
29- 30	174.7060	5.2376	(Eu)	A	I
31- 31	177.4602	5.3201	(A2u)	A	I
32- 32	186.4944	5.5910	(B1u)	I	I
33- 34	189.4772	5.6804	(Eg)	I	A
35- 36	219.0456	6.5668	(Eu)	A	I
37- 38	220.0680	6.5975	(Eg)	I	A
39- 39	226.8208	6.7999	(B2g)	I	A
40- 40	243.5099	7.3002	(B2u)	I	I
41- 42	244.0217	7.3156	(Eu)	A	I
43- 43	247.8790	7.4312	(A2u)	A	I
44- 44	281.1441	8.4285	(A2g)	I	I
45- 46	281.8829	8.4506	(Eg)	I	A
47- 47	293.2041	8.7900	(B1u)	I	I
48- 48	294.1697	8.8190	(B1g)	I	A
49- 49	295.4587	8.8576	(B2g)	I	A
50- 50	305.9358	9.1717	(A2g)	I	I
51- 52	311.5696	9.3406	(Eg)	I	A

53-	53	326.1310	9.7772	(A1g)	I	A
54-	54	340.7597	10.2157	(B2g)	I	A
55-	56	341.3371	10.2330	(Eu)	A	I
57-	57	341.9141	10.2503	(A1u)	I	I
58-	59	357.8595	10.7284	(Eu)	A	I
60-	60	363.9106	10.9098	(B1u)	I	I
61-	62	388.3722	11.6431	(Eu)	A	I
63-	63	389.7639	11.6848	(A1g)	I	A
64-	64	390.8242	11.7166	(B1g)	I	A
65-	66	391.4535	11.7355	(Eg)	I	A
67-	67	399.5929	11.9795	(B1g)	I	A
68-	68	402.6799	12.0720	(A1u)	I	I
69-	69	409.7577	12.2842	(B2g)	I	A
70-	70	420.2018	12.5973	(B2u)	I	I
71-	71	421.5555	12.6379	(A2g)	I	I
72-	72	424.9873	12.7408	(A2u)	A	I
73-	73	436.1742	13.0762	(B1u)	I	I
74-	75	442.1988	13.2568	(Eu)	A	I
76-	76	442.9534	13.2794	(B2u)	I	I
77-	78	455.4493	13.6540	(Eg)	I	A
79-	79	457.9246	13.7282	(A1g)	I	A
80-	81	458.2747	13.7387	(Eu)	A	I
82-	82	465.1333	13.9443	(A2g)	I	I
83-	84	468.1839	14.0358	(Eu)	A	I
85-	86	468.6534	14.0499	(Eg)	I	A
87-	87	478.9625	14.3589	(B1g)	I	A
88-	88	479.5446	14.3764	(A2u)	A	I
89-	90	496.8818	14.8961	(Eg)	I	A
91-	91	497.8908	14.9264	(A1u)	I	I
92-	92	504.5518	15.1261	(B1u)	I	I
93-	94	505.0469	15.1409	(Eu)	A	I
95-	95	505.1626	15.1444	(B2g)	I	A
96-	96	512.1002	15.3524	(A1g)	I	A
97-	97	514.9534	15.4379	(B1g)	I	A
98-	99	515.2771	15.4476	(Eg)	I	A
100-	100	522.6348	15.6682	(B2u)	I	I
101-	101	525.4977	15.7540	(B1u)	I	I
102-	102	531.6466	15.9384	(A2u)	A	I
103-	103	534.7110	16.0302	(A2g)	I	I
104-	105	538.0819	16.1313	(Eu)	A	I
106-	107	548.2618	16.4365	(Eg)	I	A
108-	108	549.6132	16.4770	(A1u)	I	I
109-	109	551.9066	16.5457	(B1g)	I	A
110-	111	552.0334	16.5495	(Eu)	A	I
112-	112	562.2103	16.8546	(B2g)	I	A
113-	113	563.9403	16.9065	(A2u)	A	I
114-	115	568.7039	17.0493	(Eg)	I	A
116-	116	569.1409	17.0624	(B2u)	I	I
117-	117	569.4884	17.0728	(A2g)	I	I

118- 119	575.4547	17.2517	(Eu)	A	I
120- 120	582.7248	17.4696	(A1g)	I	A
121- 121	610.5629	18.3042	(B2u)	I	I
122- 123	661.3481	19.8267	(Eu)	A	I
124- 124	669.7903	20.0798	(B1g)	I	A
125- 125	670.4179	20.0986	(A1g)	I	A
126- 127	675.1231	20.2397	(Eg)	I	A
128- 128	679.1538	20.3605	(B1u)	I	I
129- 129	680.2258	20.3927	(A1u)	I	I
130- 131	685.4180	20.5483	(Eg)	I	A

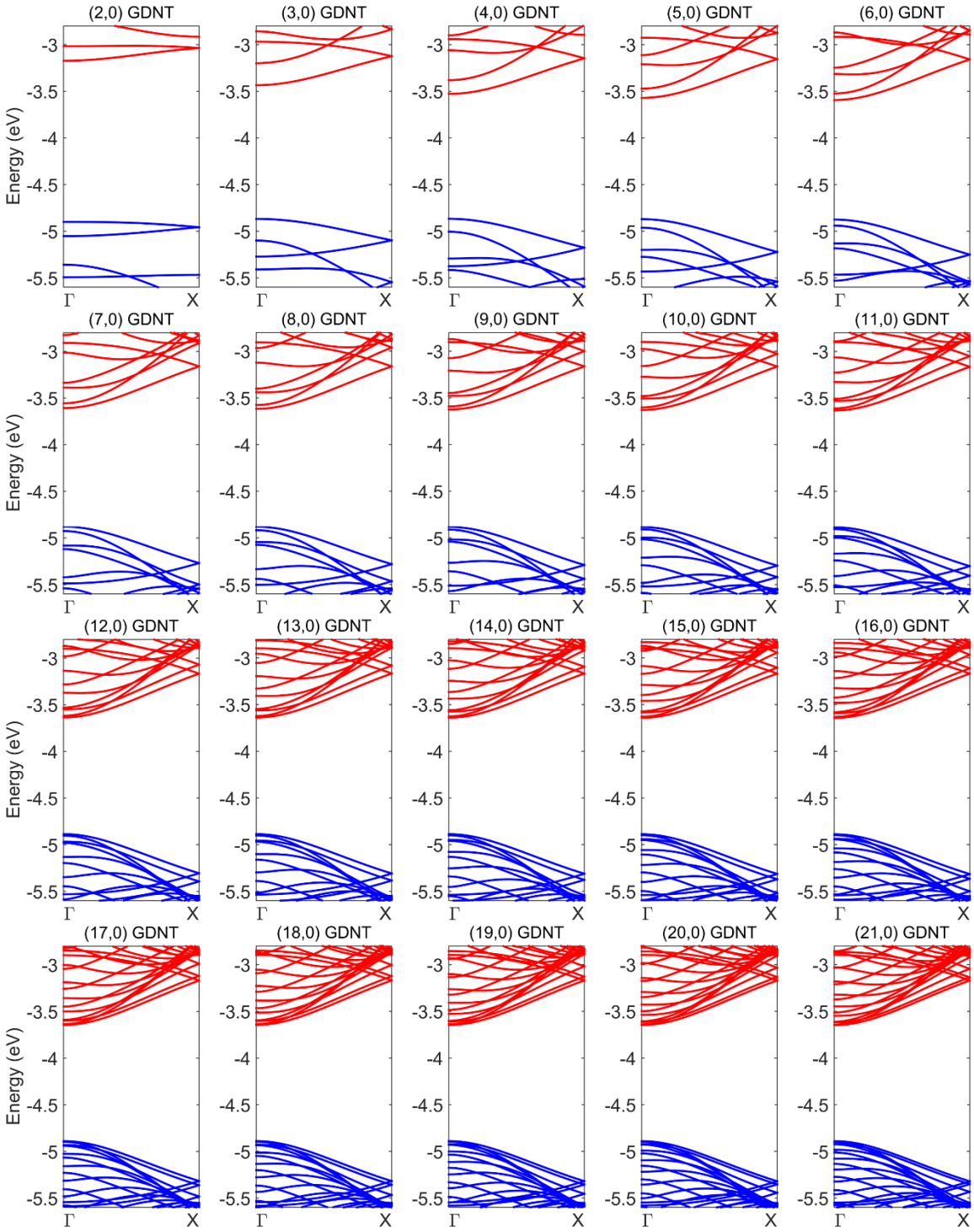

Figure 1.11. Electronic band structures (relative to vacuum at 0 eV) of various (n,0) armchair GDNTs for $n = 2 – 21$

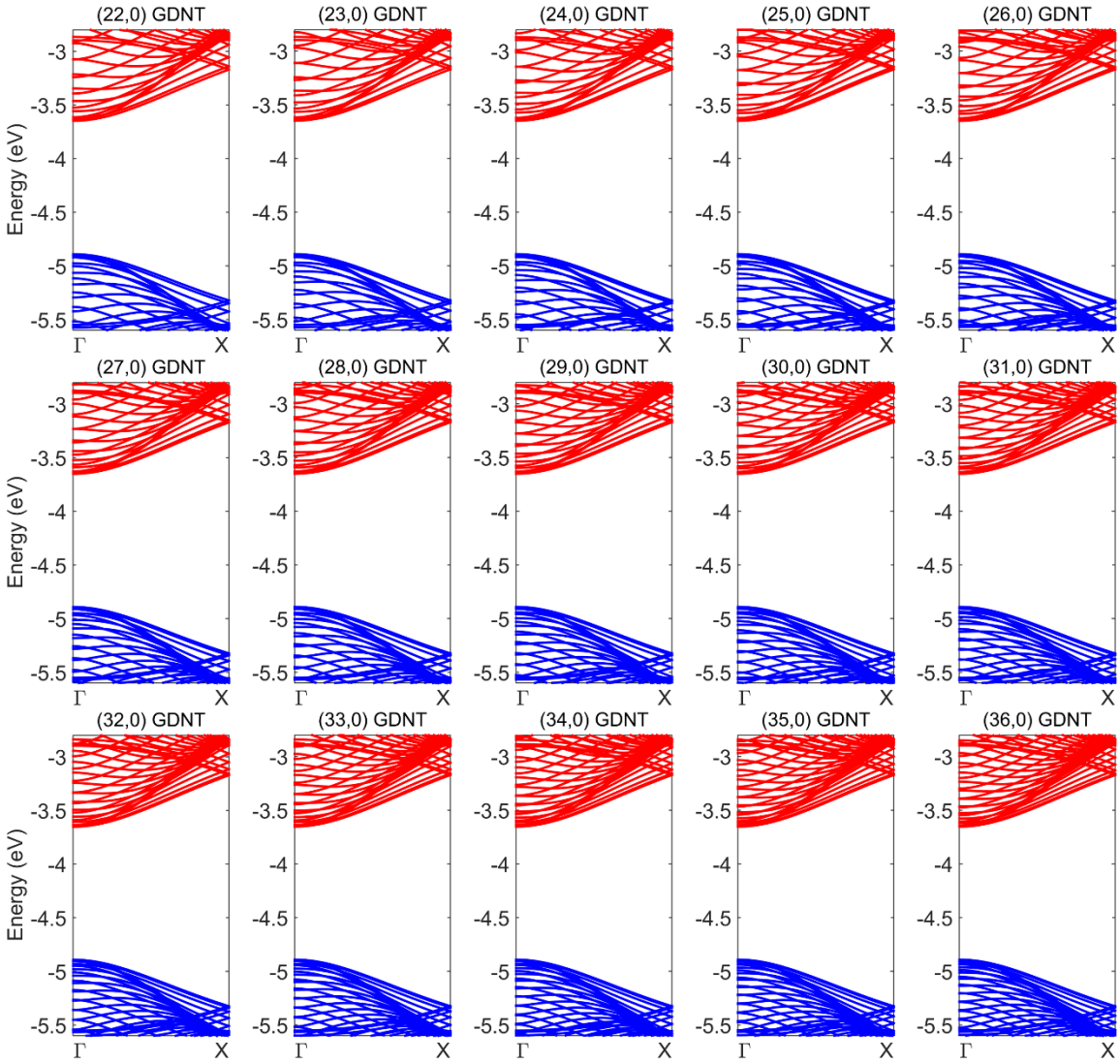

Figure 1.12. Electronic band structures (relative to vacuum at 0 eV) of various (n,0) armchair GDNTs for n = 22 – 36

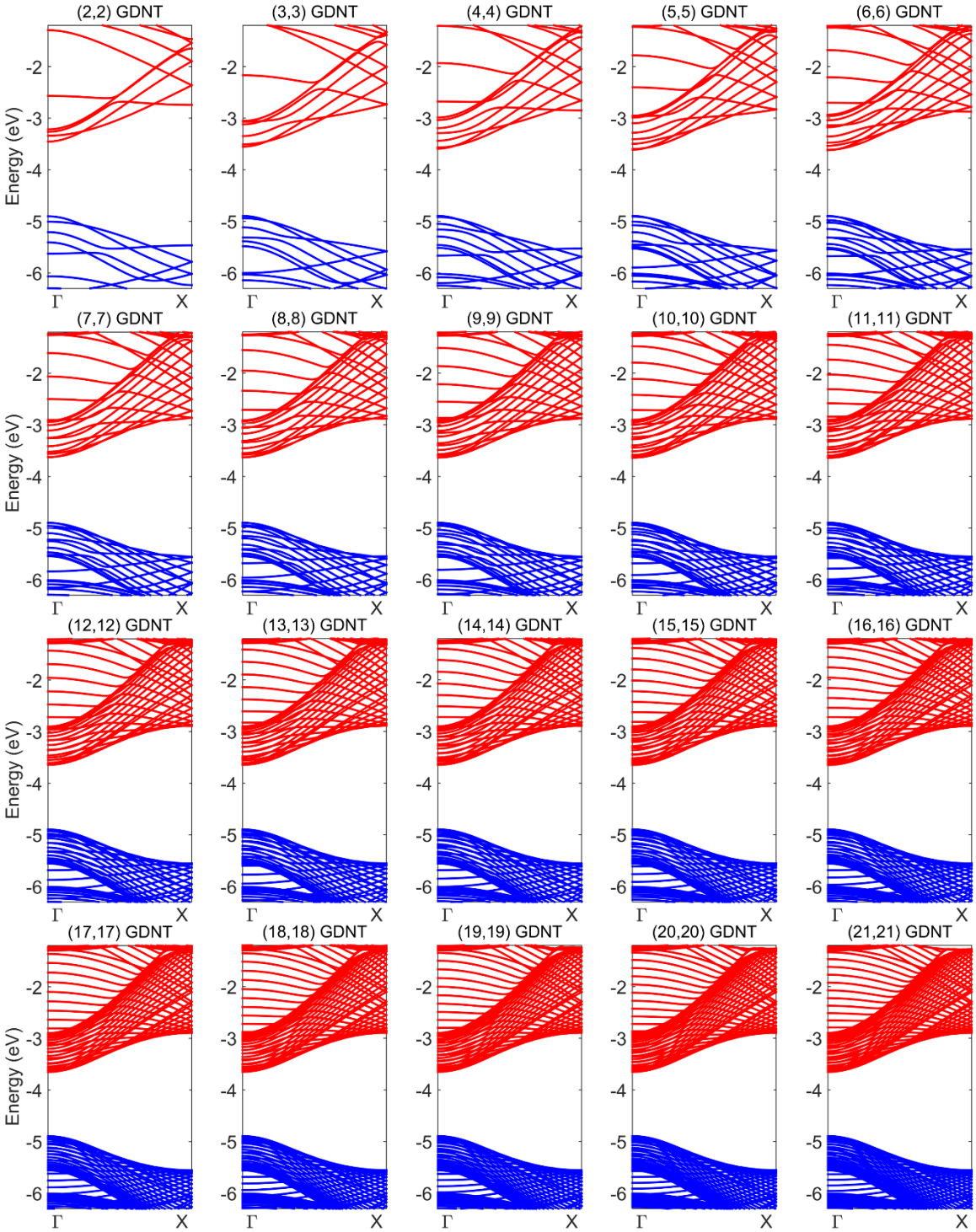

Figure 1.13. Electronic band structures (relative to vacuum at 0 eV) of various (n,n) zigzag GDNTs for $n = 2 – 21$